SPARK PLASMA SINTERING OF ALUMINUM MATRIX COMPOSITES

By

VINEET YADAV

B.E. in Mechanical Engineering

Rajiv Gandhi Technical University

Bhopal, Madhya Pradesh

2003-2007

Submitted to the Faculty of the
Graduate College of the
Oklahoma State University
in partial fulfillment of
the requirements for
the Degree of
MASTER OF SCIENCE
July, 2011

SPARK PLASMA SINTERING OF ALUMINUM MATRIX COMPOSITES

Thesis Approved:

Dr. Sandip P. Harimkar

Thesis Adviser

Dr. David A. Rubenstein

Dr. Kaan A. Kalkan

Dr. A. Gordon Emslie

Dean of the Graduate College

TABLE OF CONTENTS

Chapter Page

1. INTRODUCTION 1

1.1 Introduction.....1

1.2 Aluminum: Its Properties and Applications.....1

1.3 Aluminum Matrix Composites (AMCs) 3

1.3.1 Classification of AMCs.....3

1.3.1.1 Particle Reinforced AMCs 4

1.3.1.2 Whisker or Short-Fiber Reinforced AMCs 7

1.3.1.3 Continuous Fiber-Reinforced AMCs 9

1.3.1.4 Mono Filament Reinforced AMCs.....10

1.4 Processing of Aluminum Matrix Composites.....12

1.4.1 Powder Metallurgical Process.....13

1.4.1.1 Hot Extrusion.....14

1.4.1.2 Hot Isostatic Pressing.....15

1.4.1.3 Hot Pressing.....16

1.4.1.4 Hot Rolling.....17

1.4.1.5 Spark Plasma Sintering.....18

1.4.2 Casting 18

1.4.2.1 Die Casting.....19

Chapter Page

1.4.2.2 Squeeze Casting 19

1.4.2.3 Stir Casting.....20

1.5 Challenges in Processing Metal Matrix Composites.....21

1.6 Spark Plasma Sintering 22

1.6.1 Parameters of the Spark Plasma Sintering 24

1.6.1.1 Effect of Heating Rate 25

1.6.1.2 Effect of Temperature 26

1.6.1.3 Effect of Pressure 27

1.6.1.4 Effect of DC Pulse 28

1.7 Aluminum Matrix Composites: A Review 29

1.7.1 CNT reinforced Aluminum Composites 29

1.7.2 Ceramic reinforced Aluminum Composites 34

1.8 Objective 38

2. EXPERIMENTAL DETAILS 39

2.1 Materials 39

2.2 Experimental Procedure 40

2.2.1 Milling Process 40

2.2.2 Spark Plasma Sintering 40

2.3 Processing of Aluminum and Al-Matrix Composites.....43

2.3.1 Fabrication of Bulk Samples of Aluminum and its Composites.....43

2.4 Characterization and Testing Methods 44

2.4.1 Density Measurement 44

Chapter Page

2.4.2 Micro structural and Phase Analysis.....45

2.4.3 Wear Test.....45

2.4.4 Mechanical Testing.....46

2.4.4.1 Microhardness Testing.....46

2.4.4.2 Nanoindentation Testing.....46

2.4.4.3 Compression Testing.....47

3. RESULTS AND DISCUSSION.....48

3.1 Spark Plasma Sintering of CNT Reinforced Aluminum Composite.....48

3.1.1 Micorstructure Characterization of Al-CNT Composites.....48

3.1.2 Micro- and Nano-Mechancial Testing.....52

3.1.3 Wear Characteristics.....56

3.2 Spark Plasma Sintering of SiC Reinforced Aluminum Composite.....62

3.2.1 Micorstructure Characterization of Al-SiC Composites.....62

3.2.2 Microhardness Test.....66

3.2.3 Wear Characteristics.....67

3.3 Spark Plasma Sintering of Fe-based Metallic Glass Reinforced Aluminum Composite.....72

3.3.1 Micorstructure Characterization of Al-MG Composites.....72

3.3.2 Microhardness Test.....76

3.3.3 Wear Characteristics.....77

4. CONCLUSIONS.....82

5. FUTURE WORK.....84

Chapter Page

REFERENCES 85

APPENDICES 91

LIST OF TABLES

Table		Page
Table 1.1	Characteristics properties of aluminum [1]…….....	2
Table 1.2	Types of reinforcements used in aluminum matrix composites [2]….	4
Table 1.3	Hardness and density of Al-CNT composites [68]……..	31
Table 1.4	Typical properties of some ceramic reinforcements used in AMCs [79].....	38
Table 2.1	Specifications of the materials used in the current study…….	39

LIST OF FIGURES

Figure Page

Fig. 1.1 Microstructure of (a) aluminum matrix composites having high volume fraction of SiC particle reinforcement, (b) short fiber-reinforced aluminum matrix composite, (c) continuous fiber-reinforced aluminum matrix composite, and (d) hybrid composite containing 10% SiC and 4% graphite particles [4]……..... 5

Fig. 1.2 Fatigue crack initiation and growth in (a) monolithic 2080 Al, and (b) SiCp reinforced 2080 Al composite [5]…….……..... 6

Fig. 1.3 Initial portions of the tensile stress-strain curves of 2124 composites containing 0, 8, or 20 % SiC whiskers or particulate; strained to 0.6 % permanent set after solution heat treatment and quenching and then aged for 10 h at 145 ~ (T8) [6]……..... 8

Fig. 1.4 Fatigue fracture surfaces of Al- 45 vol.% Al_2O_3 at (a) 1200 MPa, (b) 1000 MPa, and (c) 900 MPa [9]……...…… 10

Fig. 1.5 Classification of processing of bulk aluminum matrix composites……..... 12

Fig. 1.6 Products processed by PM techniques [10]……...……..... 13

Fig. 1.7 TEM image of hot-extruded composite (a) before the compression test, and (b) after 10% deformation (carbon nanotubes are marked by black arrows)

Figure Page

[12]…….. 15

Fig. 1.8 Tensile fractographs of hot rolled (a) SiCw/Al, and (b) aluminum borate whisker ($A1_{18}B_4O_{33}$)/Al composite [23]..... 17

Fig. 1.9 Optical microstructure of squeeze casting RZ5DF-14 vol.% saffil fibers produced under (i) atmospheric pressure and, applied pressure of (ii) 20 MPa, (iii) 40 MPa, (iv) 60 MPa, (v) 80 MPa, (vi) 100 MPa and (vii) 120 MPa [33]..... 21

Fig. 1.10 Typical examples of material processed by SPS processing [40]……..... 23

Fig. 1.11 Passage of direct current flowing through the surface of the particles [43]…….. 24

Fig. 1.12 Schematic of typical SPS experiment showing the six main user-defined processing parameters: (1) heating rate, (2) maximum (hold) temperature, (3) cooling rate, (4) load application rate, (5) maximum load hold, and (6) load removal rate [44]..... 25

Fig. 1.13 Grain growth of Aluminum at different heating rates [45]……..... 26

Fig. 1.14 (a) SEM image showing fracture surface of Al-2 wt.% CNT, and (b) TEM image of Al-2 wt.% CNT [71]…… 33

Fig. 1.15 SEM of etched spark plasma sintered (a) Al-CNT (2.5 wt.%), and (b) Al-CNT (5 wt.%) composite [72]…… 33

Fig. 1.16 SEM images of composites heated at 1100 ºC and cooled at a rate of 10 ºC/min (a) 1-3 µm TiC particles size and (b) 2-10 µm TiC particles size [78]…….. 36

Figure Page

Fig. 1.17 SEM images of composites heated (a) at 1100 ºC for 1 hour and cooled by taking out of the furnace rapidly, (b) at a rate of 5 ºC/min, and (c) 2 ºC/min [78]……..... 37

Fig. 2.1 Different components of spark plasma sintering equipment in the OSU laboratory…… 42

Fig. 2.2 Position of thermocouple inside the graphite die and punch inside SPS setup…… 43

Fig. 2.3 Schematic of fabrication of Al-matrix composites using ball mill and spark plasma sintering…….……. 44

Fig. 3.1 SEM images from (a) starting aluminum powder, (b) spark plasma sintered aluminum, (c) ball milled Al-CNT powder mixture, and (d) spark plasma sintered Al-CNT composites……... 48

Fig. 3.2 X-ray diffraction patterns from spark plasma sintered (a) aluminum, and (b) Al-CNT composites……..……... 50

Fig. 3.3 EDS spectrum and corresponding elemental composition of Al-CNT composites……... 51

Fig. 3.4 Representative compressive stress-strain curves of spark plasma sintered aluminum and Al-CNT composites…….……..... 52

Fig. 3.5 Typical nanoindentation load-displacement curves for aluminum and Al-CNT composites obtained with peak loads of (a) 100 μN, and (b) 200 μN……. 54

Fig. 3.6 Typical images of nanoindentation impressions and associated depth profiles for (a) aluminum, and (b) Al-CNT composites (nanoindentation peak load of

Figure Page

9000 μN)……. 56

Fig. 3.7 Cumulative weight loss as a function of sliding time during ball-on-disc wear testing conducted with normal force of 1N for Al and Al-CNT composites….. 57

Fig. 3.8 (a) surface profiles of wear tracks, and (b) line profiles across the wear tracks for aluminum and Al-CNT composites…….. 58

Fig. 3.9 Variation of coefficient of friction with sliding time during ball-on-disc wear testing conducted with normal force of 1N for aluminum and Al-CNT composites……... 59

Fig. 3.10 SEM images from the worn surfaces of (a-b) aluminum, and (c-d) Al-CNT composites……... 60

Fig. 3.11 SEM images of spark plasma sintered Al-SiC composites (a) 5 wt.% , (b) 10 wt.%, and (c) 20 wt.% SiC..... 63

Fig. 3.12 EDS of Al-SiC composites with reinforcements of 5, 10, and 20 wt.% SiC….. 64

Fig. 3.13 Relative densities of Al-SiC composites with reinforcement of 5, 10, and 20 wt.% SiC…….. 65

Fig. 3.14 X-ray diffraction patterns from spark plasma sintered Al-SiC composites with reinforcement of 5, 10 and 20 wt.% SiC..... 66

Fig. 3.15 Vickers micro-hardness of spark plasma sintered Al-SiC composites with reinforcement of 5, 10 and 20 wt.% SiC..... 67

Fig. 3.16 Weight loss as a function of sliding time during ball-on-disc wear testing conducted with normal force of 4 N for aluminum and Al-SiC composites….. 68

Figure Page

Fig. 3.17 Variation of coefficient of friction with sliding time (10 min) during ball-on-disc wear testing conducted with normal force of 4 N for aluminum and Al-SiC composites…….. 69

Fig. 3.18 Surface profiles of wear tracks of Al-SiC composites (a) pure aluminum (b) 5wt%, (c) 10 wt.%, and (d) 20 wt.% SiC..... 70

Fig. 3.19 SEM images of wear track of spark plasma sintered Al-SiC composites with reinforcement of (a-b) 5 wt.% , (c-d) 10 wt.%, and (e-f) 20 wt.% SiC…….. 71

Fig. 3.20 SEM images of spark plasma sintered Al-MG composites (a-b) 5 wt.% , (c-d) 10 wt.%, and (e-f) 20 wt.% MG..... 73

Fig. 3.21 Line scans analysis of interface between aluminum and MG particles…….. 74

Fig. 3.22 Area scans analysis of interface between aluminum and MG particles…….. 74

Fig. 3.23 Relative densities of Al-MG composites with reinforcement of 5, 10 and 20 wt.% MG..... 75

Fig. 3.24 X-ray diffraction patterns from spark plasma sintered Al-MG composites with reinforcement of 5, 10 and 20 wt.% MG..... 76

Fig. 3.25 Vickers microhardness of Al-MG composites with reinforcement of 5, 10 and 20 wt.% MG..... 77

Fig. 3.26 Weight loss as a function of sliding time during ball-on-disc wear testing conducted with normal force of 4 N for aluminum and Al-MG composites….. 78

Fig. 3.27 Variation of coefficient of friction with sliding time (10 min) during ball-on-disc wear testing conducted with normal force of 4 N for aluminum and Al-MG composites……... 79

Figure Page

Fig. 3.28 Surface profiles of wear tracks of Al-MG composites (a) pure aluminum (b) 5wt%, (c) 10 wt.%, and (d) 20 wt.% MG..... 80

Fig. 3.29 SEM images of wear track of spark plasma sintered Al-MG composites (a-b) 5 wt.% , (c-d) 10 wt.%, and (e-f) 20 wt.% MG..... 81

CHAPTER 1

INTRODUCTION

1.1 Introduction

Aluminum is well known for its light weight and high strength applications. However, there are efforts to improve its properties by making aluminum matrix composites (AMCs). Reinforcing aluminum with hard phases leads to strengthening of the composites. However, there are challenges associated with processing of metal matrix composites like dispersion of the reinforcement and achieving high interfacial strength. In this thesis, various reinforcements like multi-wall carbon nanotubes (MWCNTs), silicon carbide (SiC), and Fe-based metallic glass (MG) were used to process AMCs using spark plasma sintering (SPS). SPS is a novel technique where DC pulse and uniaxial current are used to obtain fully dense AMCs. Various characterizations including phase analysis, microstructural analysis, and multiscale mechanical characterizations were performed.

1.2 Aluminum: Its Properties and Applications

Aluminum is the most abundant metal on the Earth's crust and the third most common element, after silicon and oxygen. By utilizing various combinations of its advantageous properties like strength, lightweight, corrosion resistance, recyclability, and formability, aluminum is being used in ever-increasing number of applications [1]. The products

range from structural materials through thin packing foils. Aluminum naturally generates a protective oxide layer and which is highly corrosion resistant. Different types of surface treatment like anodizing, painting, or lacquering can further improve this property which is very useful for applications where protection and conservation are required.

Table 1.1 Typical properties of aluminum [1]

Property	Value
Density (solid)	2699 Kg m^{-3} (theoretical density based on lattice spacing
Coefficient of expansion	$23X10^{-6}$ K^{-1} at 293 K
Thermal conductivity	2.37 W cm^{-1} K^{-1} at 298 K
Melting point	933.5 K
Yield strength	7-11 MPa
Vickers hardness	167 MPa
Young's modulus	70 GPa
Shear modulus	26 GPa

Efforts are made to manufacture light weight and component in both aerospace and automobile industry. Though, the excessive demands of advanced applications also need new materials which are stronger, lightweight, and can acquire higher temperature capabilities. Aluminum is good for net shape manufacturing routes which open possibilities for advanced applications [1]. Most of the applications of aluminum metal are given as follows:

1. Structural applications
2. Electrical transmission lines

3. Aerospace industries
4. Automotive industries
5. Space craft
6. Telescope mirrors
7. Food and beverages packaging
8. Kitchen utensils

1.3 Aluminum Matrix Composites (AMCs)

A composite material consists of two or more constituent materials with considerably different physical and/or chemical properties [2]. The composite has better characteristic properties than those of each of the individual component. Generally, the reinforcement component is dispersed in the continuous matrix component. AMCs are developed to provide properties such as high strength, stiffness, wear resistance, machinability, high thermal conductivity, and a low coefficient of thermal expansion [3]. In the last few decades, emphasis is given on processing and development of advanced AMCs in order to support the recent commercial applications.

1.3.1 Classification of AMCs

AMCs are generally distinguished by characteristics of their reinforcement. Reinforcements can be produced in the form of short fibers, continuous fibers, whiskers or particles. These are categorized by the diameter and aspect ratio (ratio of length to diameter or thickness) of the reinforcement. Aspect ratio plays a crucial role as the degree of load transfer from the matrix to the reinforcement is directly proportional to the

reinforcement aspect ratio. Table 1.2 shows typical examples of important reinforcements used in metal-matrix composites.

Table 1.2 Types of reinforcements used in aluminum matrix composites [2]

Type	Aspect ratio	Diameter	Examples
Particle	~1-4	1-25	SiC, Al_2O_3, BN, B_4C
Short fiber or whisker	~10-1000	0.1-25	SiC, Al_2O_3, Al_2O_3 + SiO_2, C
Continuous fiber	>1000	3-150	SiC, Al_2O_3, C, B, W

There are four types of AMCs, depending on the type of reinforcement [4]

(a) Particle reinforced AMCs

(b) Whisker or short fiber-reinforced AMCs

(c) Continuous fiber-reinforced AMCs

(d) Mono filament-reinforced AMCs

1.3.1.1 Particle Reinforced Aluminum Matrix Composites (PAMCs)

Particle reinforced AMCs are one of the largest quantities of composites formed and utilized on a volume and weight basis [4]. These are produced by techniques like powder metallurgy (PM) stir cast, melt infiltration, spraying, and in situ processing techniques at an industrial level. Ceramic reinforcements are generally oxides, carbides or borides and these ceramics are present in a volume fraction less than 30% in case of structural and wear resistance applications. PAMCs have been successfully used as components in automotive, aerospace, and opto-mechanical assemblies. PAMCs are used as a fan exit guide vane in the gas turbine engine, as ventral fins, and fuel access cover doors in

military aircraft. PAMCs are also used in helicopters as rotating blade sleeves. Fig. 1.1(a) shows the microstructure of cast aluminum matrix composite having high volume fraction SiC particle reinforcements.

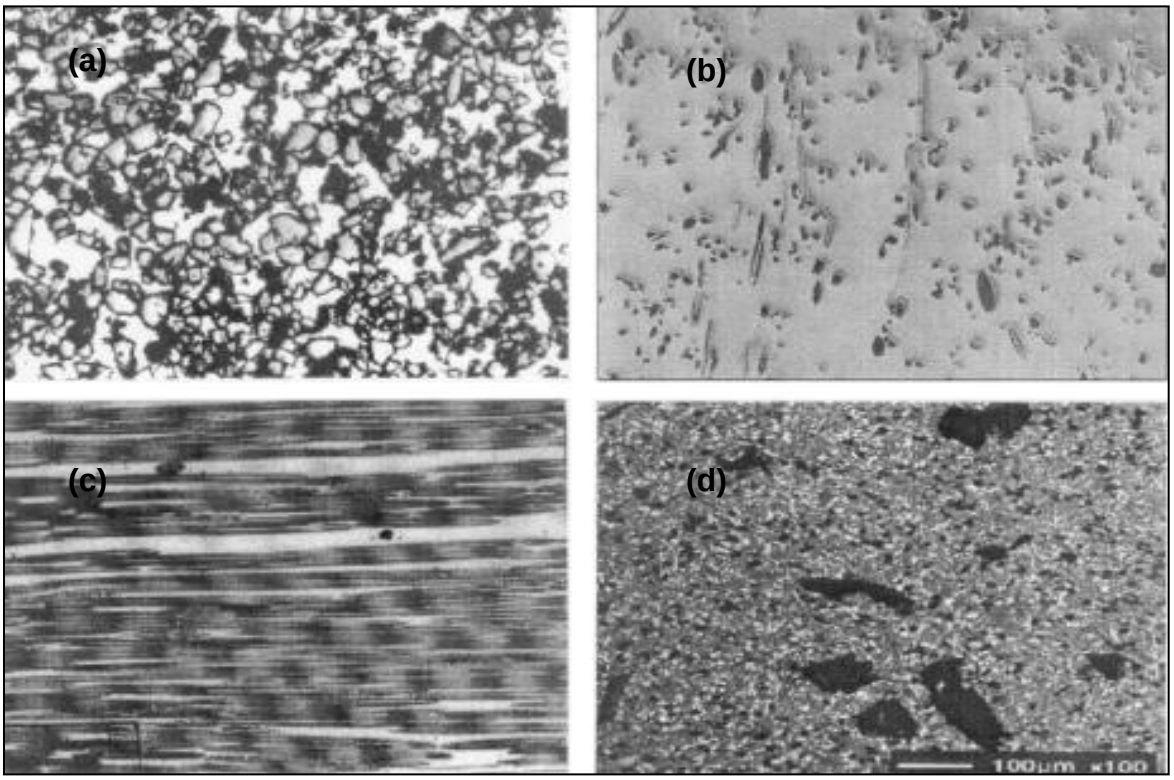

Fig. 1.1 Microstructure of (a) aluminum matrix composites having high volume fraction of SiC particle reinforcement, (b) short fiber-reinforced aluminum matrix composite, (c) continuous fiber-reinforced aluminum matrix composite, (d) hybrid composite containing 10% SiC and 4% graphite particles [4]

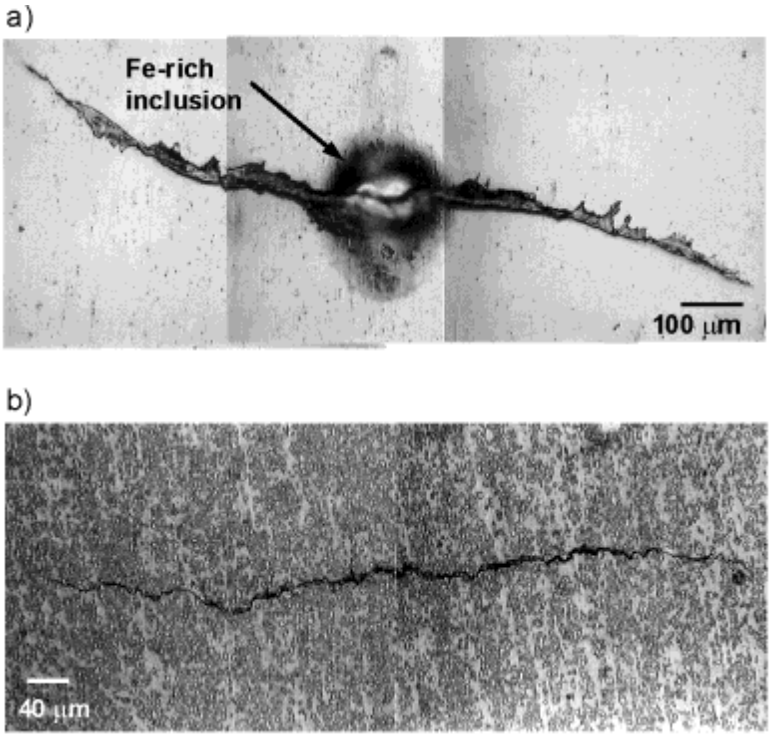

Fig. 1.2 Fatigue crack initiation and growth in (a) monolithic 2080 Al, and (b) SiCp reinforced 2080 Al composite [5]

Particle reinforced aluminum matrix composites (PAMCs) are attractive due to their less expensive processing cost and their homogenous properties throughout the structure. They can be processed using similar techniques as used by monolithic metals. Strengthening due to reinforcement of particles can be explained using classical composite strengthening. During loading, matrix transfers the load to the reinforcement, and these stiffer reinforcements carry the applied load on the total structure. This is also termed as a direct strengthening mechanism. There is also indirect strengthening due to particle reinforcement [5]. There is a difference between the thermal conductivities of the metal matrix and reinforcement particles which leads to a formation of dislocations during solidification or the thermal hardening processes, resulting in indirect

strengthening. Fig. 1.2 shows a fatigue failure of pure 2080 Al alloys and the effect of SiC reinforcement on crack propagation in composite. It is evident that crack growth is restricted due to crack deflection or crack trapping. Presence of SiC particulates in the matrix resulted in increase of fatigue strength as they hinder the crack propagation.

1.3.1.2 Whisker or Short Fiber Reinforced Aluminum Matrix Composites

Different strengthening mechanisms due to reinforcement using short fibers are direct strengthening, residual thermal stress in fibers, matrix work hardening due to dispersion of fibers, and thermal stress induced dislocations strengthening [6]. Direct fiber reinforced strengthening is the dominating mechanism when compared to other mentioned mechanisms. Under tensile loading conditions, fibers which are inclined in the direction of a matrix or having little inclination take the maximum load and reach their ultimate strength and fail. Then the load is transferred to the fibers which are having higher inclination angles. Residual thermal strengthening plays a crucial role which occurs due to the difference in the coefficient of thermal expansion. Papazian and Adler investigated the effect of SiC particles as well as fibers in aluminum metal matrix, and it was observed that short fibers are more effective as reinforcement when compared to particles [7]. As shown in the Fig. 1.3, increase in reinforcement results in increase in tensile strength, and short fibers are a more effective reinforcement than particles.

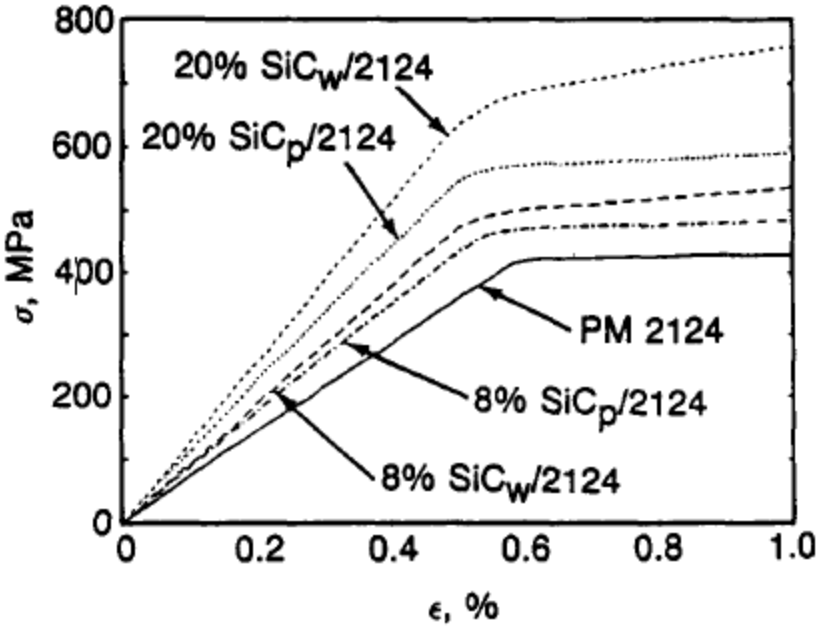

Fig. 1.3 Initial portions of the tensile stress-strain curves of 2124 composites containing 0, 8, or 20 % SiC whiskers or particulate; strained to 0.6 % permanent set after solution heat treatment and quenching and then aged for 10 h at 145 ~ (T8) [6]

These types of composites contain reinforcements with an aspect ratio of greater than 5 but are not continuous. These are one of the first and most popular which has potential application in pistons. Fig. 1.1(b) shows the microstructure of short fiber reinforced AMCs. Mechanical properties of whisker reinforced composites are better compared to particle or short fiber reinforced composites. Nevertheless, in the recent years, usage of whiskers as reinforcements in AMCs is vanishing because of apparent physical condition hazards. Short fiber reinforced AMCs exhibit uniqueness in between that of continuous fiber and particle reinforced AMCs [7-8].

1.3.1.3 Continuous Fiber Reinforced Aluminum Matrix Composites

In continuous fiber reinforced aluminum matrix composites, the reinforcement is in the form of continuous fibers such as alumina, SiC, or carbon with a diameter of less than 20 μm. The fibers can either be parallel, pre-woven, or braided prior to the production of the composite. AMCs having a fiber volume fraction up to 40% are produced by the squeeze infiltration technique. These composites are produced by a pressure infiltration route. Fig. 1.1(c) shows the microstructure of continuous fiber (alumina) reinforced AMCs.

Continuous fiber based aluminum matrix composites are known for strengthening in the direction of fiber alignment; however, less strength is observed in other directions. When tensile loading is applied on continuous fiber reinforced composite, initially both matrix and fiber deform elastically until the matrix starts deforming plastically. At this point, reinforced fibers start taking maximum loads and a point comes where these fibers start breaking one by one. Fig. 1.4 shows a fatigue fracture surface of alumina fiber reinforced aluminum matrix. The fracture surface clearly shows fracture of alumina fibers before failure of the composite. Fiber pullout and kinking of the fibers are a few mechanisms which occur during fracture of these kinds of composites. The strong interface between fiber and matrix is extremely important for high strength of continuous fiber reinforced aluminum matrix composites [9].

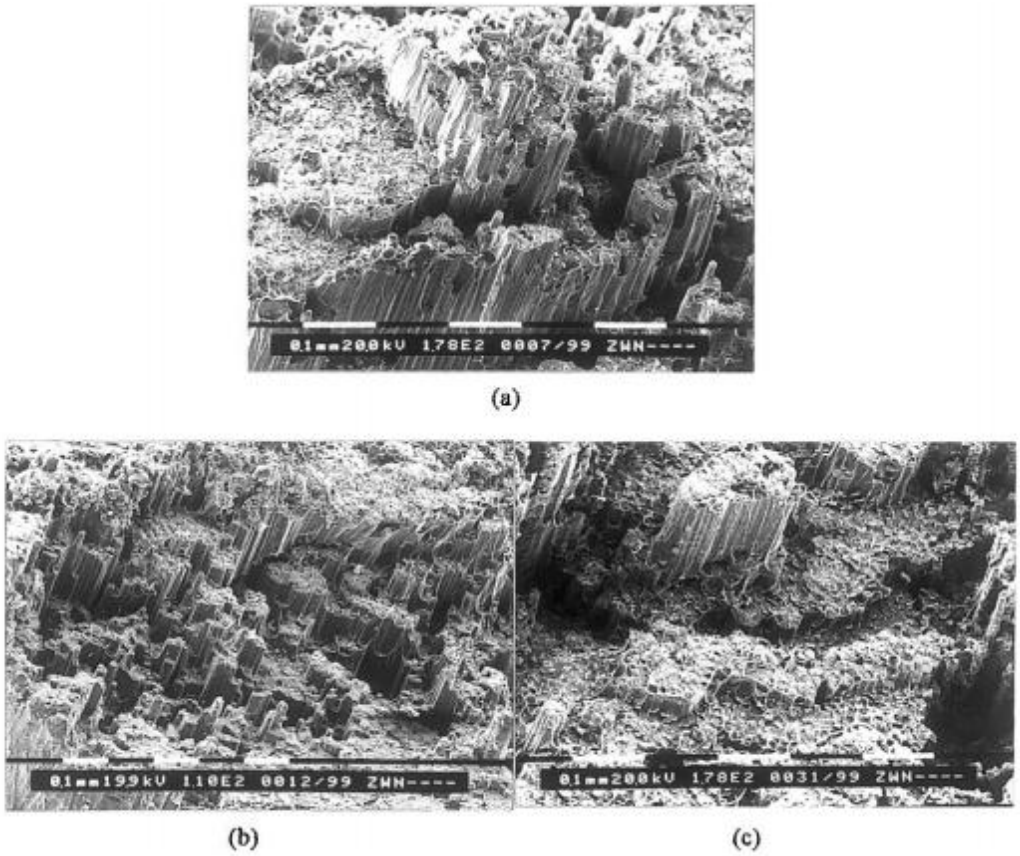

Fig. 1.4 Fatigue fracture surfaces of Al-Al_2O_3 (45 vol.%) (a) at 1200, (b) at 1000, and (c) at 900 MPa [9]

1.3.1.4 Monofilament Reinforced Aluminum Matrix Composites (MFAMCs)

Monofilaments are large diameter (100 to 150 μm) fibers, generally formed by chemical vapor deposition (CVD) of either SiC or B into a core of carbon fiber or tungsten (W) wire. Bending flexibility of monofilaments is low compared to multifilaments. Monofilament reinforced aluminum matrix composites are produced by diffusion bonding techniques and is limited to super plastic forming aluminum alloy matrices. In

continuous fiber reinforced aluminum matrix composites (CFAMCs) and monofilament reinforced aluminum matrix composites (MFAMCs), the reinforcement is the principal load-bearing constituent, and the role of the aluminum matrix is to bond the reinforcement, transfer, and distribute loads. These composites exhibit directionality. Low strength in the direction perpendicular to the fiber orientation is distinguishing of CFAMCs and MFAMCs. In particle and whisker-reinforced AMCs, the matrix is the major load-bearing constituent. The role of the reinforcement is to strengthen and stiffen the composite by preventing matrix deformation by mechanical restraint. In addition to four types of AMCs described above, another variant of AMCs known as hybrid AMCs have been developed and are in use to some extent. Hybrid AMCs basically contain more than one type of reinforcement. For example, a mixture of particle and whisker, a mixture of fiber and particle, or a mixture of hard and soft are common types of reinforcements [4]. Aluminum matrix composite containing a mixture of carbon fiber and alumina particles used in cylindrical linear applications is an example of a hybrid composite. Fig. 1.1(d) shows a microstructure of hybrid AMC having both hard SiC and soft graphite particles as reinforcement.

1.4 Processing of Aluminum Matrix Composites

Aluminum matrix composites can be processed by numerous techniques. Some of these important techniques are described below.

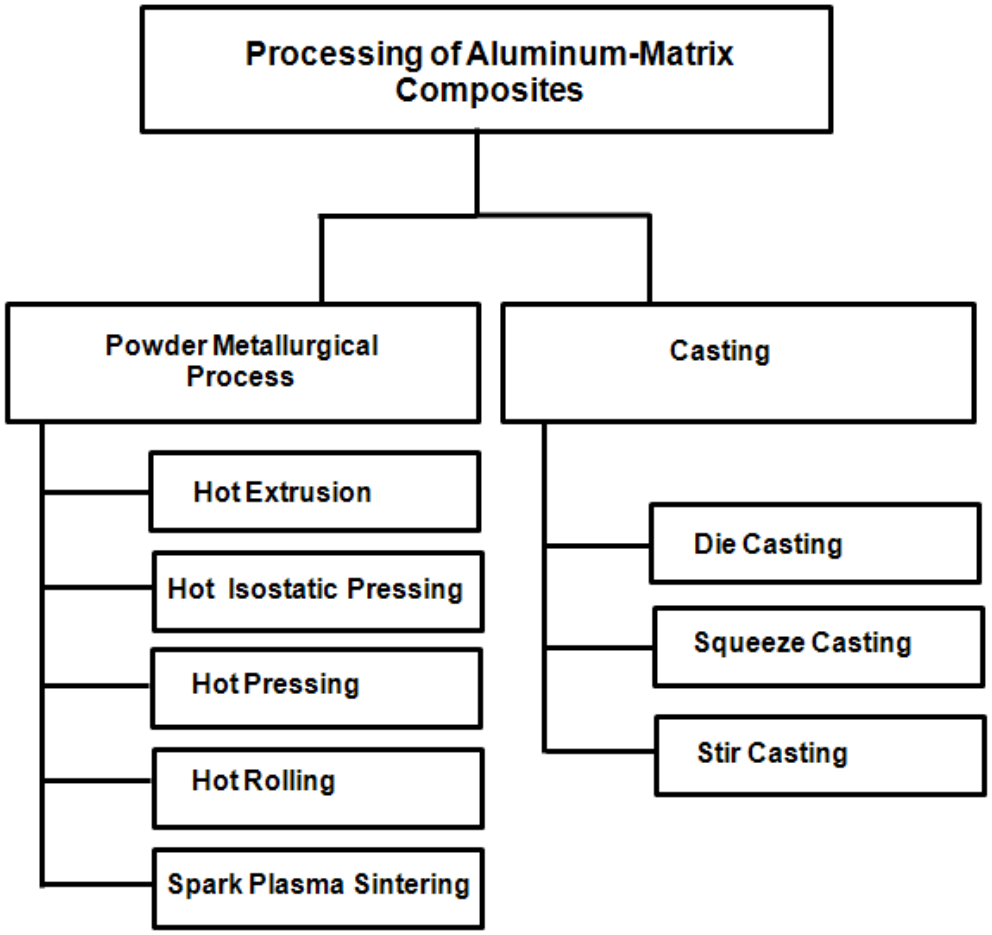

Fig. 1.5 Classification of processing of bulk aluminum matrix composites

Fig. 1.5 shows classification of various processing techniques. Basically processing techniques used for AMCs can be classified into casting and powder metallurgical routes. This section reviews a few of these processes.

1.4.1 Powder Metallurgical (PM) Process

Powder metallurgy is a highly advanced method used to process reliable components using elemental or pre alloyed powders using heat and pressure in controlled atmosphere. PM is one of the most versatile and flexible metal forming techniques, having the ability to process a wide spectrum of materials including conventional alloys, immiscible systems, ceramics, and composites which are difficult to process by conventional methods. Powder metallurgical processes are used in a wide range of industries, from automotive and aerospace applications to power tools and household appliances. Fig. 1.6 shows some of the net shaped products processed by the PM technique. This section describes various powder metallurgy routes and their application in processing Al-based composites.

Fig. 1.6 Products processed by PM techniques [10]

1.4.1.1 Hot Extrusion

Hot extrusion is the conventional technique to process both ferrous and non-ferrous materials. This process is generally performed at high temperatures above the recrystallization temperature. Extrusion has been used to process different shapes like rods, strips, and tubes with desirable lengths [11].

Researchers have used only the hot extrusion process for fabrication of materials [12] and also used it with the spark plasma sintering process [13-14]. It is well established that classical metal forming methods as secondary processing of the discontinuously reinforced composites can lead to break up of particle agglomerates, improved bonding, and the reduction or removal of porosity. These all are the properties which contribute to improve the mechanical properties of AMCs [15]. Hot extrusion has been used as one of the most common secondary processing due to its excellent preferential axial alignment of discontinuous fibers and large compressive hydrostatic stress rate [16].

Choi *et al.* [12] reported the fabrication of a ball milled mixture of aluminum powder and carbon nanotubes followed by hot extrusion. In these studies, two different grain sizes of aluminum (200 and 76 nm) were used. It showed significant improvement in yield stress as the grain size was reduced. Aluminum with grain size 76 nm showed higher yield stress (283 MPa) than aluminum of 200 nm grain size (238 MPa). The dependence of grain size on yield stress matched with the Hall-Petch equation. Young's modulus of Al-CNT composite (104.19 GPa) and the aluminum (70.05) with grain size of 200 nm were showed. Significant improvements in Young's modulus of composite were exhibited by the reinforcement of carbon nanotubes in aluminum matrix.

Liao *et al.* [13] processed Al-MWCNTs composites using spark plasma sintering followed by hot extrusion. The hot extrusion process was carried out for making the cylindrical rod of 10 mm diameter for testing the tensile behavior.

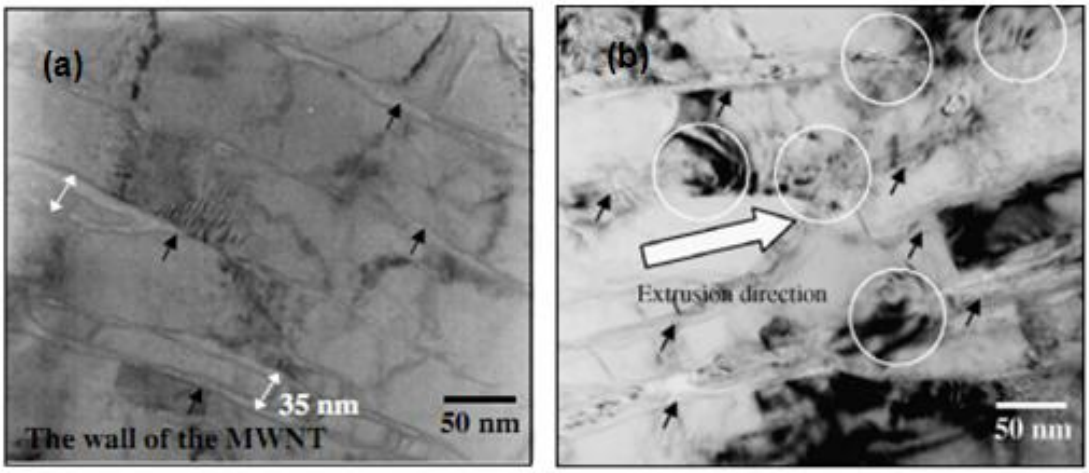

Fig. 1.7 TEM image of hot-extruded composite (a) before the compression test (b) after 10% deformation (carbon nanotubes are marked by black arrows) [12]

1.4.1.2 Hot Isostatic Pressing (HIP)

Hot isostatic pressing involves high hydrostatic pressure and a high temperature to compact fine particles into bulk samples. Hot isostatic pressing is used widely to process metal matrix composites. Zulphia *et al.* [17] investigated HIP of aluminum casting alloy A357 with 15 vol.% SiC particles at constant pressure (103 MPa) and two different temperatures (535 & 565 °C). Hot isostatic pressing resulted into increase in the bending yield strength, bending moment, and bend nominal strength by 10-30%. Atkinson *et al.* [18] reported the effect of hot isostatic pressing treatments on the porosity of aluminum casting alloy A357 and stir-cast A357/15 vol% SiC particulate metal matrix composites. This resulted in the significant decrement in the relative porosity.

Xu *et al.* [19] reported the hot isostatic pressing of cast SiC particulate reinforced Al composites at different temperatures and pressures. To observe the effects of the HIP method, microstructures and tensile properties of Al-SiC composite were characterized on the casted and HIPed sample. It was observed that ductility of casted composites was increased significantly after treating HIP. After the T6 treatment, the HIPed samples were superior to the casted samples in terms of strength as well as in ductility. It might be due to the increment in density level and matrix softening.

1.4.1.3 Hot Pressing

Hot Pressing is an alternative method to process metal and ceramic compacts to full density with a controlled microstructure. It is a process where heat and uniaxial pressure is used to compact different materials. Researchers have used hot pressing to process high strength composites.

Roy *et al.* [20] used the hot pressing for the processing of materials, such as Fe-aluminide and alumina reinforced aluminum matrix composites. Hot pressing resulted into the in-situ reaction occuring between molten aluminum and Fe_2O_3 powder containing nanosized crystallites. The in-situ reaction between molten aluminum and Fe_2O_3 occured at a temperature above the melting point of aluminum (~660 °C), which forms Fe-aluminides and Al_2O_3 in the composite samples. Fe_3Al-CNT composites were also fabricated using hot pressing which exhibited improved mechanical properties such as hardness, compressive strength and bend strength due to uniform dispersion of CNTs.

1.4.1.4 Hot Rolling

Hot rolling is an extensively used method for the forming of discontinuous reinforced aluminum matrix composites [21]. Hot rolling involves thermo mechanical processing where processing at high temperature results into decrease of the required energy and to increase the workability of metal being rolled. [22].

Fei *et al.* [23] reported the reinforcement of silicon carbide and aluminum borate whiskers in aluminum matrix composites, processed using hot rolling at 550 °C. Fig. 1.8 showed the elongation for SiCw/Al and aluminum borate whisker ($A1_{18}B_4O_{33}$)/Al has increased significantly. Formation of small dimples can be observed which are mainly due to failure of the matrix. Bigger voids were also observed which results of crack formation due to hot rolling.

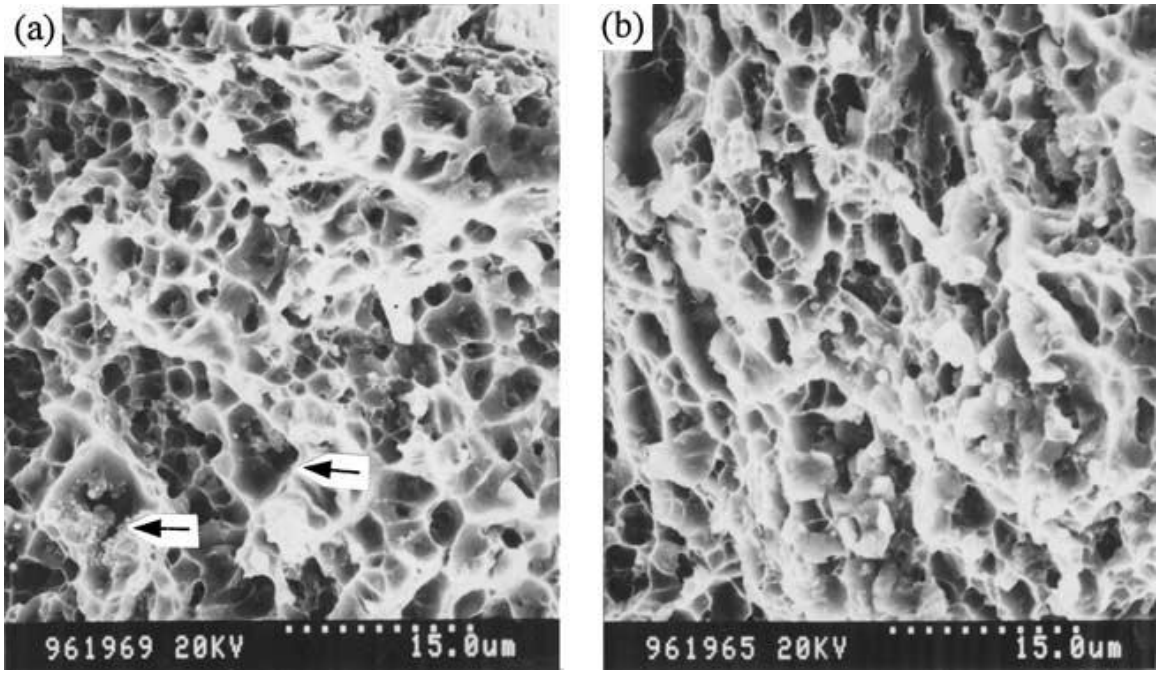

Fig. 1.8 Tensile fractographs of hot rolled SiCw/Al (a) and aluminum borate whisker ($A1_{18}B_4O_{33}$)/Al (b) composites [23]

Xu *et al.* [24] reported the hot rolling of aluminum borate whisker-reinforced 6061 aluminum alloy composite with different reductions. The evolution of texture in aluminum borate whisker ($A1_{18}B_4O_{33}$)/6061Al composite using the hot rolling technique is distinguished from that of monolithic aluminum alloys, which showed the effect of the whiskers in the composite.

1.4.1.5 Spark Plasma Sintering

Spark plasma sintering is a novel sintering technique which involves pulsed direct current and uniaxial pressure. Detailed discussion is presented in the later section.

1.4.2 Casting

Casting is the most economical technique of making metallic components in which liquid melt is poured into the mold or pattern of the required dimensions. There are many processing defects of the casting process such as porosity, segregation, hot tears, and formation of hydrides and oxides etc. [25]. To minimize these casting defects, modifications are made in the casting processes, which are known as die casting, stir casting, and squeeze casting etc.

In the casting of metal matrix composites, the particulates such as ceramic particulates are integrated into a molten metal matrix using a variety of proprietary techniques, which is followed by the mixing and casting of the resulting metal matrix composites [26]. This section briefly presents various casting techniques used for processing aluminum matrix composite.

1.4.2.1 Die Casting

Among other manufacturing techniques (squeeze casting, compo castings, continuous casting, and stirring casting, the die casting technique is most suitable to obtain economic parts of near-net shape metal matrix composites [27].

Li *et al.* [28] reported the CNT reinforced aluminum matrix composites processed by high pressure die casting. It is observed that the light metal matrix composites showed significant improvement by adding only a small amount of CNTs. Studies revealed that a simple procedure like high pressure die casting can be used to process Al reinforced CNTs. Tensile test represents the tensile strength of Al/CNT composites increased (8%), and elongation at the fracture has increased (27%) compared to pure aluminum alloy.

1.4.2.2 Squeeze Casting

The squeeze casting process is a special casting technique which involves processing of both ferrous and non-ferrous metals besides composites. It has the combined advantages of high pressure die casting, gravity permanent mold die casting, and common forging technology [29].

Yong and Clegg [30] investigated that the combination of applied pressure and preform preheat temperature for the squeeze casting of Mg based alloy was determined to be 80 MPa and 600 °C, respectively. For this combination, an ultimate tensile strength value of 259 MPa was reported. Fig. 1.9 shows the optical micrographs of squeeze casting magnesium alloy metal matrix composite containing 14 vol.% saffil fibers formed under with different applied pressures (from 0.1-120 MPa). SEM images represent the

effect of applied pressure on the cast structure. An examination of the optical micrographs structure shows the porosity in samples produced with applied pressure below 60 MPa. At an applied pressure greater than 80 MPa, the micrographs show the tendency for fracture and fiber clustering. It is also demonstrated that the expected porosity took place mainly at cell boundaries, and by adjusting the depth of the field, it was easily confirmed.

Sukumaran *et al.* [25] studied that the Al 2124 alloy and Al 2124-10SiCp composite using squeeze cast to get the microstructure and mechanical properties comparable with that observed by hot working.

1.4.2.3 Stir Casting

Stir casting is the technique for the manufacturing of discontinuous metal matrix composites. It is simple, flexible, and useful in large scale production. Also, it gives near-net shape formation of the composites [31] and provides a conventional metal processing route, which minimizes the final cost of the product [32].

Rajan *et al.* [33] reported the effect of three different liquid stir casting processes (compocasting, modified compocasting, and modified compocasting followed by squeeze casting) on the properties and structure of fine fly ash particles reinforced Al-7Si-0.35 Mg alloy composite (shown in Fig. 1.9). Among all liquid stir castings, modified compocasting followed by a squeeze casting route exhibit good dispersion of fly ash particles.

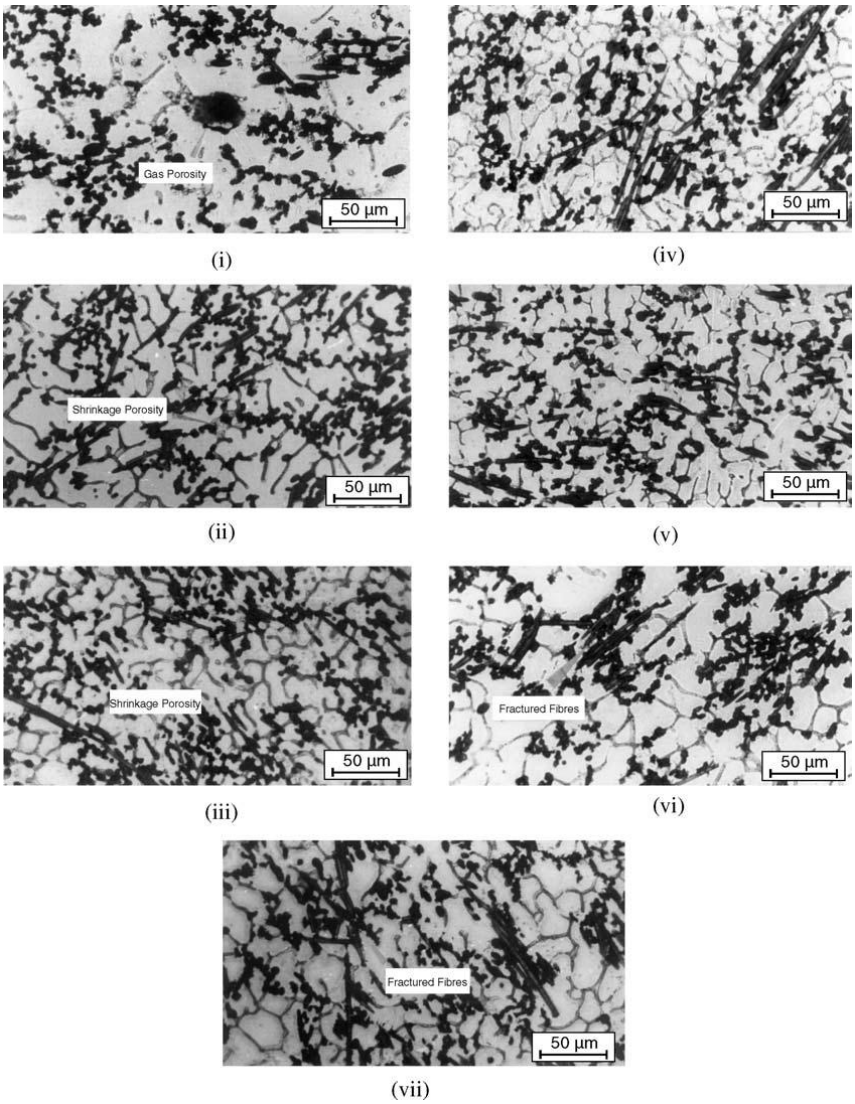

Fig. 1.9 Optical microstructure of squeeze casting of Mg-based alloy (RZ5DF) -14 vol.% saffil fibers produced under (i) atmospheric pressure, applied pressure of (ii) 20 MPa, (iii) 40 MPa, (iv) 60 MPa, (v) 80 MPa, (vi) 100 MPa, and (vii) 120 MPa [33]

1.5 Challenges in Making Aluminum Matrix Composites

The two main challenges in aluminum matrix composites are using appropriate reinforcement which can improve the properties and simultaneously nanostructuring the metal matrix which can strengthen the composite using Hall-Petch effect. Different class

and length scale of reinforcements were discussed in detail in above sections. One of the challenges which occur during reinforcement is dispersion of particulates throughout the matrix. Uniform dispersion of the reinforcement plays a significant role in improving the properties as well as for obtaining homogeneous properties [34]. Researchers reported the decrease in mechanical, electrical, and thermal properties of the composites due to clustering phenomena [35-38]. Significant improvement has been reported because of enhancement in dispersion.

One of the main critical challenges is the suitable design of the interface between the matrix and the particles (from micron sized to nano sized particles). The overall interfacial area also increases significantly when surface or volume ratio increase going to nanosized fillers, which plays an important role. In order to attain high strength and better thermal property of aluminum matrix composites, strong interfacial bonding and low thermal resistance between reinforcement and matrix is required.

Nano structuring of aluminum matrix composite is equally significant which results in strengthening of composites. However, it is difficult to confine the grain growth to nano scale during processing. Different techniques like high heating and cooling rates, high pressure and grain growth inhibitors were used to control the grain growth; however processing nano structured fully dense is still a challenge.

1.6 Spark Plasma Sintering

Spark plasma sintering (SPS) is a new sintering technique, which includes high pulsed direct current and uniaxial pressure to consolidate the materials. The SPS technique has high heating and cooling rates which are up to 1000 K/min, and the processing time is

also very fast i.e. few minutes [39]. Hence, the SPS process is appropriate to fabricate functionally graded materials (FGMs), intermetallic compounds, fiber reinforced ceramics (FRC), metal matrix composites (MMC), and nanocrystalline material [40]. Fig. 1.10 shows the typical examples of material which can be sintered by the SPS process.

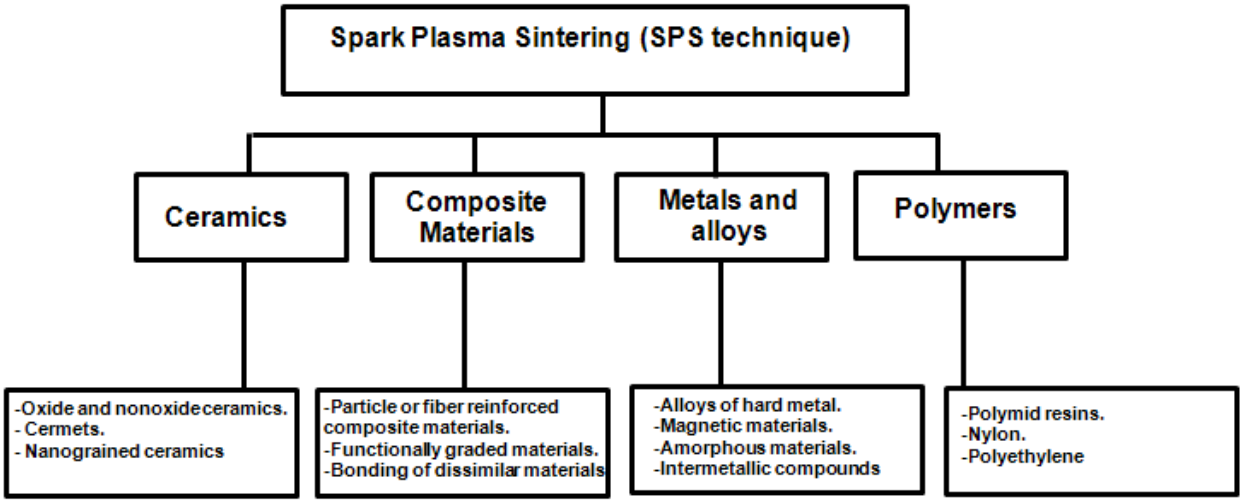

Fig. 1.10 Typical examples of material processed by SPS processing [40]

During the SPS process, the DC pulse voltage and current create spark discharge and joule heating points between particles of powder through the die (graphite or tungsten) and sample, while a pressure is applied on the powder, as shown in Fig. 1.11 [41]. Joule heating provides high heating rates which can provide a benefit by by-passing the grain coarsening low temperature mechanism i.e. surface diffusion [42]. The SPS technique has the capacity of achieving nearly 100% theoretical density in almost any metallurgical or ceramic material and composites [41].

Past research concluded that the SPS technique formed materials with particularly improved properties. Improvement in mechanical properties, oxidation and corrosion

resistance, optical transmission, microstructure, and electrical properties has been reported [42].

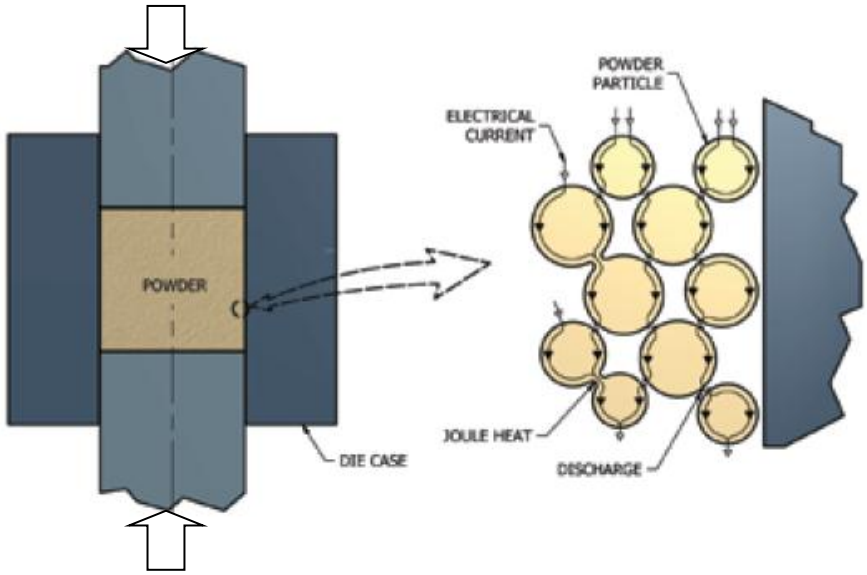

Fig. 1.11 Passage of direct current flowing through the surface of the particles [43]

1.6.1 Parameters of the Spark Plasma Sintering

An SPS technique has its own advantages in the range of controllability of its processing parameters. The basic parameters of the SPS technique include heating rate, sintering temperature, cooling rate, pressure rate, maximum load hold, and load removal rate (as shown in Fig. 1.12) [42, 44]. Discussion is being done on the parameters of the SPS technique, which is related to obtaining a dense sample and the result of the microstructure characterization of the materials.

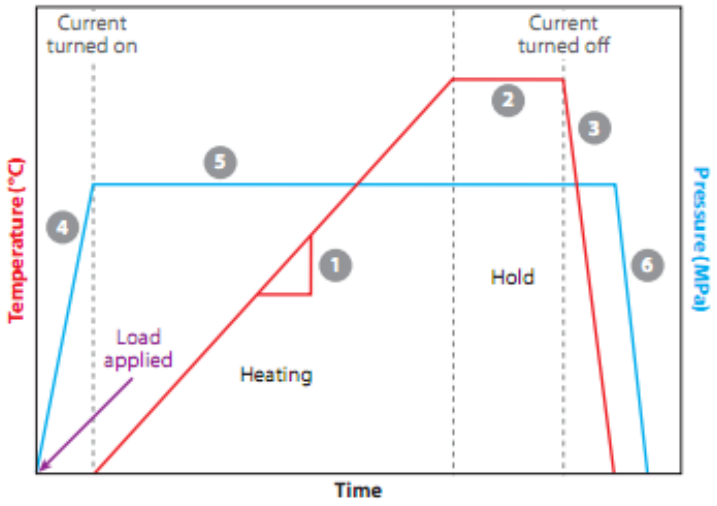

Fig. 1.12 Schematic of typical SPS experiment showing the six main user-defined processing parameters: (1) heating rate, (2) maximum (hold) temperature, (3) cooling rate, (4) load application rate, (5) maximum load hold, and (6) load removal rate [44]

1.6.1.1 Effect of Heating Rate

High heating rate is one of the dominant parameter of spark plasma sintering which differentiates it from other conventional sintering techniques. Three different mechanisms, surface diffusion, grain boundary diffusion and power-law creep, heating rate influence the grain boundary diffusion which increases sinterability. Olevsky *et al.* [45] investigated the constitutive modeling applied to spark plasma sintering of aluminum and substantiated it with experimental investigations. Fig. 1.13 shows dependency of grain growth on heating rate. It was observed that, higher heating rates can be used to restrain the grain growth. It was also observed that reduced particle size enhances the heating rate effect on consolidation of aluminum.

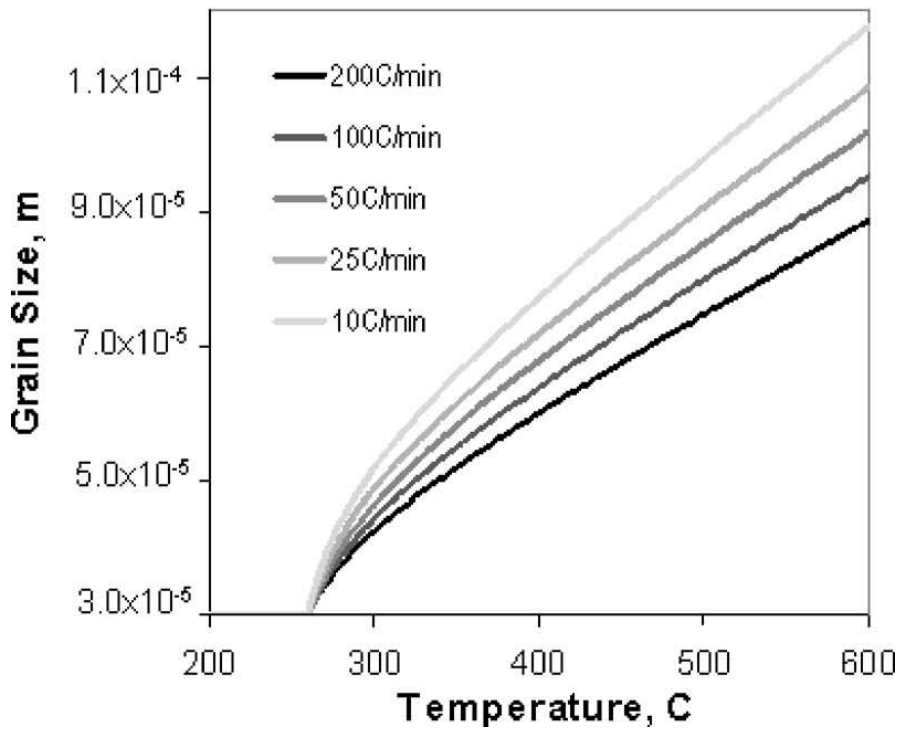

Fig. 1.13 Grain growth of Aluminum at different heating rates [45]

1.6.1.2 Effect of Temperature

The effect of temperature plays a significant role in powder densification, which requires mass transfer and is consequently estimated by temperature dependent.

In SPS, all the heat comes from the flowing current in the form of joule heat with a heat generation rate (q), which is given by the equation,

$$Q = J\,E \qquad (1.1)$$

where, J is the current density, and E is the electric field.

Garay *et al.* introduced the linear curve fit for the density and temperature relationship,

$$\rho = s\,(T/T_m) + b \qquad (1.2)$$

Where, ρ is relative density, s is slope; also termed as temperature sensitivity, T is processing temperature, T_m is melting temperature, and b is the intercept on density axis. Temperature sensitivities of oxides and carbides are between 1.5 and 3, while for metals, it varies from 0.5 to 1. Higher temperature sensitivity means the material's density is dependent on temperature. Lower temperature sensitivity of metals is because of a higher plastic deformation than ceramics, and current effects such as electro migration may be useful in the densification process [44].

1.6.1.3 Effect of Pressure

Effect of pressure on densification during spark plasma sintering is well established. There are two effects of pressure on sintering: a mechanical effect and an intrinsic effect. In the mechanical effect pressure works in a rearrangement of particles and in breaking of agglomeration. In the intrinsic effect, the pressure can be evaluated by the driving force of sintering [42].

$$\frac{d\rho}{(1-\rho)dt} = B\left(g\frac{\gamma}{x} + P\right) \quad \text{.....(1.3)}$$

Where, ρ = Fractional density,

B = Consists of diffusion coefficient and temperature

g = Geometric constant

γ = Surface energy

x = Particle size scale

t = Time

P = Applied external pressure

The first term on the RHS of the equation represents the intrinsic driving force for sintering, whereas the second term shows the intrinsic contribution to the driving force by the applied pressure.

1.6.1.4 Effect of Direct Current Pulse

Presence of DC pulsing in SPS makes it significantly unique from other conventional sintering technique. Different mechanisms proposed due to presence of DC pulsing is generation of spark during in between the powder surface and cleansing effect which reduces the oxide layer on the powder. However, these mechanisms are still under investigation and no further conclusions were drawn based on these proposed mechanisms. Researchers have used various routes like theoretical analysis, numerical modeling, as well as studies of effect of DC pulsing on various properties of spark plasma sintered materials. Xie *et al.* [46] studied the effect of pulse rating on densification of aluminum powder. No significant effects were observed on the densification of aluminum powder due to the variation of pulse frequency ranging from 0 to 300 kHz. U. Anselmi-Tamburini [47] studied the effect of pulsing and its direction on in-situ spark plasma sintering. It was observed that pulse DC current direction has no influence on solid state reactivity; however, the reaction rate decreases in the absence of DC pulse. More fundamental investigations are required to understand the complete effect of DC pulsing on various phenomenons during spark plasma sintering.

1.7 Aluminum Matrix Composites: A Review

In this section, fabrication of aluminum matrix composites using different processing methods is being discussed. In the reported experiments, researchers have tried to include different variations in content of reinforcements. Fabrication of aluminum matrix composites is performed by the powder metallurgy route followed by spark plasma sintering or a hot deformation method.

Aluminum matrix composites make a distinct category of advanced engineering materials that provide unique properties and advantages over conventional Al alloys. In general, these materials exhibit higher hardness, stiffness, and strength as well as good wear and corrosion resistance. Other main characteristic properties are the coefficient of thermal expansion (CTE) and the dimensional stability of the composites, which can be modified by controlling the reinforcement type, size, morphology, and relative quantity.

1.7.1. CNT reinforced Aluminum Composites

Carbon nanotubes (CNTs) exhibit excellent combination of mechanical, electrical, thermal, and chemical properties. Since the discovery of CNTs in 1991, significant efforts have been directed towards utilizing these useful properties in a wide range of applications, including structural, electronic, health, defense, and energy applications [48-52]. The CNTs are also evolving as important large aspect ratio reinforcement/filler materials for improving strength, stiffness, toughness, and high temperature stability of structural materials such as polymers, metals/alloys, and ceramics [53-59]. The CNTs are particularly attractive for strengthening structural light metals and alloys (aluminum-, magnesium-, and titanium-based alloys). As light weight and corrosion resistant

aluminum and its alloys are important materials for automotive, aerospace, and structural applications, most of the current efforts are focused on investigating the strengthening effects of CNT reinforcement in these alloys [56-59].

Various solidification processing and solid state sintering approaches have been investigated for the processing of CNT reinforced aluminum matrix composites. Early studies investigated direct injection of CNTs in the aluminum alloy melt followed by solidification of the composite casting [60-61]. However, issues related with the wettability and agglomeration of CNTs in the melt makes the processing of composites with uniformly distributed CNTs very challenging. Some efforts have been made to improve the distribution of CNTs in the cast composites by injecting CNT-coated particles (of matrix material) in the melt instead of direct injection of CNTs [61]. However, issues related to insufficient penetration of CNT-coated particles in the melt are important to achieve uniform distribution of CNTs throughout the casting. Significant efforts have been made to process CNT reinforced aluminum matrix composites using thermal/plasma spray techniques (coating technologies) [62-63]. In most of these investigations, starting powder feedstock was prepared by spray drying of the aqueous slurry containing aluminum alloy powder and CNTs. The thermal spraying of the spray dried powder resulted in fairly uniform dispersion of CNTs in the composite coatings with some extent of distributed clustering of CNTs [62]. While the thermal spray techniques are capable for producing thick (as thick as 5 mm) coatings, the processing presents significant challenges in achieving full densification and for bulk net shaping of intricate parts. Post-thermal spray densification is often required to achieve desired density in the composite coatings.

Solid-state processing of CNT reinforced aluminum matrix composites is also attracting significant interests due to the potential of achieving high density, uniform CNT dispersion, and net shaping with these processing approaches. Several processes such as cold isostatic compaction, hot pressing, hot extrusion, or combination of these processes have been investigated for the fabrication of CNT reinforced aluminum matrix composites [64-71]. For example, Choi *et al.* [67] investigated fabrication of multi-walled carbon nanotubes (MWCNTs) reinforced aluminum composites using hot extrusion of ball-milled Al-4 vol.% CNT powder mixtures. Significant increase in the yield strength and elastic modulus was reported with the CNT reinforcement (4 vol.% CNT) in the aluminum matrix. Jiang el al. [68] also reported fabrication of Al-CNT composites with 0-3 wt.% CNTs using hot pressing of the Al-CNT mixtures (produced by hand grinding). The hot pressing was conducted at 600 °C for 1 h. It was observed that 2 wt.% CNT resulted in highest increase in hardness of the composite (~54 HV). Further increase in CNT content (>2 wt.%) resulted in decrease in hardness due to agglomeration of CNTs in the composites, as shown in Table 1.3.

Table 1.3 Hardness and density of Al-CNT composites [68]

CNT content (%)	Relative density (%)	Hardness (HV)
0	97.8	29.9
0.5	95.2	40.9
1.0	94.6	50.3
2.0	94.4	54.0
3.0	93.8	38.0

Recently, Perez-Bustamante *et al.* [69] reported processing of Al-CNT composites using pressure consolidation (2 min. at 950 MPa) of ball-milled powder mixture followed by pressure-less sintering at 550 °C for 3 h. While the density of the Al-CNT composites was relatively lower (94.3-99.1% relative density), significant improvement in the yield strength of the composite was reported. The investigation also found some amorphization of the outer shells of the CNTs. Esawi *et al.* [71] also reported fabrication of Al-CNT composites with 0-5 wt.% CNTs using combination of ball milling, compaction, and hot extrusion processing. While the ball milling allowed fairly uniform dispersion of CNTs, some clustering of CNTs was also observed for Al-2 wt.% CNT composites, as shown in Fig 1.14.

At higher CNT content (Al-5 wt.% CNT), pronounced interfacial reaction with formation of Al_4C_3 was reported. It can be seen that the conventional powder processing and/or thermomechanical processing methods, in general, resulted improvement in mechanical properties of Al-CNT composites with relatively lower CNT content (~2 wt.%). However, there still exist issues related to poor densification, agglomeration of CNTs, and undesirable interfacial reactions with these techniques.

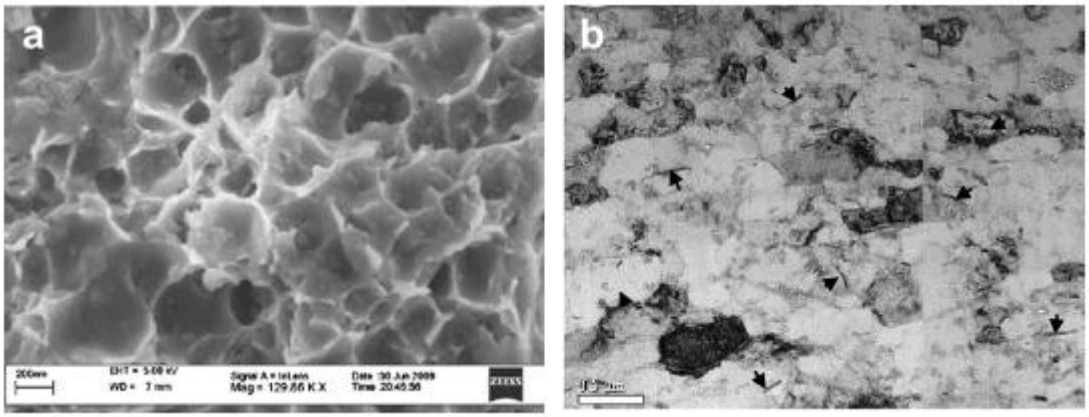

Fig. 1.14 (a) SEM image showing fracture surface of Al-2 wt.% CNT, and (b) TEM image of Al-2 wt.% CNT [71]

Morsi *et al.* [72] reported about SPS processing of Al-CNT composites (with 2.5 and 5 wt.% CNTs) using ball milled powder mixture. SEM images of etched spark plasma sintered Al-CNT (2.5 and 5.0 wt.%) composites are shown in Fig. 1.15. About 17% increase in hardness (from 91 to 107 HV) with increasing CNT content from 2.5 to 5 wt.% was reported. The spark plasma sintered composite samples also exhibited minor residual porosities.

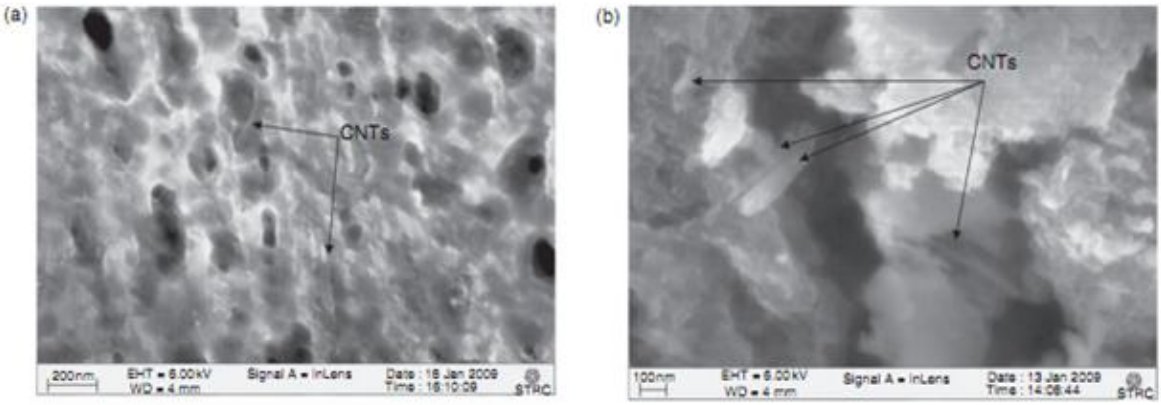

Fig. 1.15 SEM images of etched spark plasma sinterd (a) Al-CNT (2.5 wt.%), and (b) Al-CNT (5 wt.%) composite [72]

Jin-Zhi *et al.* [73] also reported fabrication of Al-CNT composites (with up to 2 wt.% CNTs) using SPS of blended powder mixture followed by hot extrusion. The improvement in the hardness with CNT reinforcement was not significant (~10%) due to pronounced agglomeration of CNTs in the composites. Morsi *et al.* [74] also investigated the effect of spark plasma extrusion (modified SPS process to allow extrusion during SPS) on the mechanical properties of the Al-2.5 wt.% CNT composites. They reported higher hardness (~33%) for the Al-CNT composites. It is clear that the dispersion of CNTs in the starting powder mixture is important to gain the advantages of SPS processing. Furthermore, most of these investigations reported effect of CNT reinforcement on microhardness of the composites. Due to multi-scale microstructures of these Al-CNT composites, it is important to understand the length-scale dependence of hardness. It is also important understand other properties; especially wear properties, of these spark plasma sintered Al-CNT composite before their potential utilization in structural applications.

1.7.2 Ceramic reinforced Aluminum Composites

Metal matrix reinforced with ceramic particles has been developed in last few decades for various light weight applications. Different particles like SiC, Al_2O_3, TiB_2, B_4C, and TiC were investigated as potential reinforcement for aluminum. Reinforcing aluminum with various ceramic particulates leads to increase of elastic modulus, hardness, tensile strength and wear resistance of the composites [75].

Surappa *et al.* [76] reported that cast aluminum-alumina, aluminum-illite, and aluminum-silicon carbide composites can be formed using the vortex method of

dispersion of powders followed by casting of the composite melts into suitable moulds. Due to addition of alumina particles (3 wt.%) in the aluminum matrix, tensile strength increases from 75.50 MN m^{-2} to 93.15 MN m^{-2}, and hardness increases from 27 BHN to 37 BHN. Also, the adhesive wear of alumina decreases from $3.62x10^{-8}$ to 2.0x10-8 cm^3 cm^{-1}. Among metal-ceramic particle composites, aluminum-alumina particle composites can possess improved wear resistance, high-temperature hardness and strength, which can be used for several applications.

Mohanty *et al.* [77] reported the fabrication of boron carbide reinforced (up to 25 wt.%) aluminum matrix composites using uniaxial pressure. The results concluded the modulus of composite depends mostly on the weight percentage of reinforcement rather than wetting at the interface. Wetting can be confirmed by judicious heat treatment in a solid state, which will decrease the embrittlement of the AMC. With an increase of the reinforcement from 0-25 wt.%, there is significant improvement in hardness (50-550 HV) and modulus of the composite is increased from 22 GPa to 183 GPa.

Hashimoto *et al.* [78] discussed the Al-TiC composite fabricated by consolidating the powder mixture by applying heat. The effects of the particle size (1-3 and 2-10 µm) of TiC and the cooling rate effect of the composites on the microstructure were reported. Al-TiC composites with 1-3 and 2-5 µm TiC particles were heated at 1100 ºC and the cooled with a cooling rate of 10 ºC/min (shown in Fig. 1.16). In Fig. 1.17, SEM images represented the thread like aluminum for both particles size. However, there was more thread like aluminum with 2-10 µm particles size. The thread like structure grew with the slowing cooling rate. Though in rapid cooling, formation of a thread-like structure was not observed.

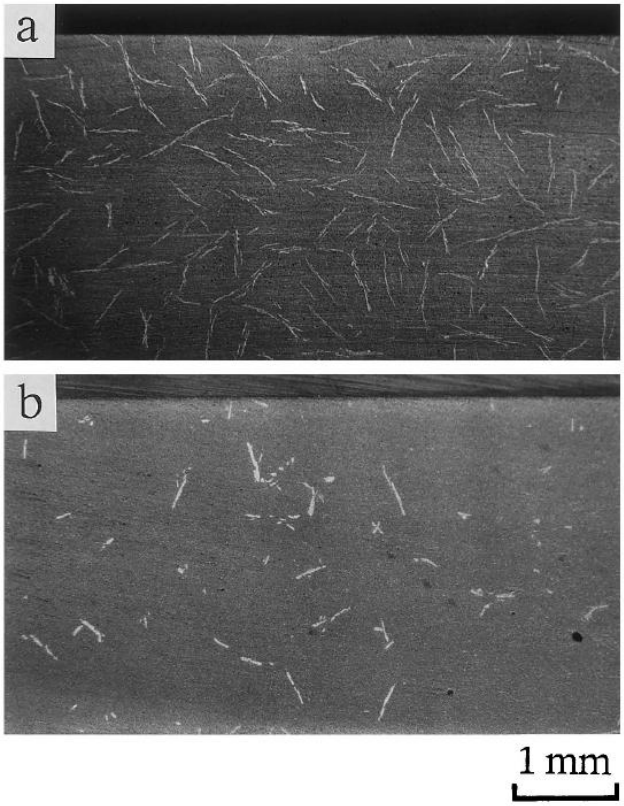

Fig. 1.16 SEM images of composites heated at 1100 ºC and cooled at a rate of 10 ºC/min (a) 1-3 µm TiC particles size and (b) 2-10 µm TiC particles size [78]

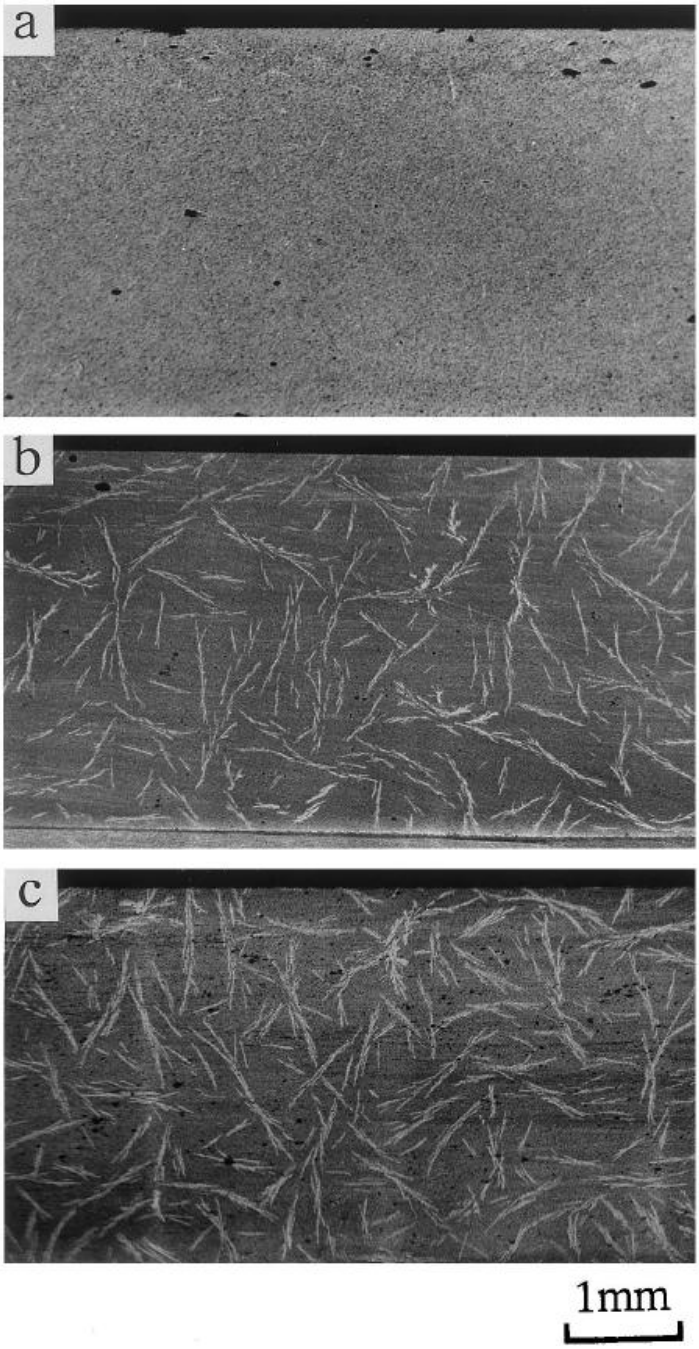

Fig. 1.17 SEM images of composites heated (a) at 1100 ºC for 1 hour and cooled by taking out of the furnace rapidly, (b) at a rate of 5 ºC/min, and (c) 2 ºC/min [78]

Table 1.4 Typical properties of some ceramic reinforcements used in AMCs [79]

Reinforcement	Coefficient of thermal expansion (10^{-6} /K)	Density (g/cc)	Elastic modulus (GPa)	Thermal conductivity (W/mK)	Ultimate tensile strength (MPa)
Al_2O_3, short fibers	-	3.29	300	-	2000
B_4C, fibers	3.5	2.35	425	39	2690
SiC fibers	-	3.46	450	-	2280
SiC particulates	3.4	3.21	448	120	-
AlN	3.3	3.26	310-345	150	2100
Si_3N_4	1.5	3.80	207	28	-

1.8 Objective

Spark plasma sintering (processing), microstructure investigation, tribological studies, and mechanical testing of

- Pure aluminum
- Al-2 wt. % MWCNTs composite.
- Al-Fe-based metallic glass composite with the reinforcements of 5, 10, and 20 wt. % metallic glass (MG).
- Al-SiC composite with the reinforcements of 5, 10, and 20 wt. % SiC.

CHAPTER 2

EXPERIMENTAL DETAILS

2.1 Materials

In current studies, 99.7 % pure Al with an average particle size of 10-40 µm, multi-wall carbon nanotubes (MWCNTs) with a particle size of 30-50 nm average diameter, and 10-20 µm length, silicon carbide (SiC) with a particle size of 2 µm, and Fe-based metallic glass having a composition of $Fe_{48}Cr_{15}Mo_{14}Y_2C_{15}B_6$, and a size less than 25 µm were used (as shown in the Table 2.1).

Table 2.1 Specifications of the materials used in the current study

Materials	Density (g/cc)	Average Size
Aluminum (Matrix)	2.7	10-40 µm
Carbon Nanotubes	2.1	length: 20 µm; diameter: 30-50 nm
Silicon Carbide	3.2	2 µm
Fe-based Metallic Glass ($Fe_{48}Cr_{15}Mo_{14}Y_2C_{15}B_6$)	7.7	25 µm

2.2 Experiment Procedure

2.2.1 Milling Process

The milling process of aluminum with other reinforcement particles is done using a high speed vibrating ball mill. Aluminum with its respective reinforcement material such as MWCNTs, SiC, and Fe-based metallic glass were placed in a 125 ml tungsten mixing jar containing 50 tungsten milling balls of 10 mm diameter (with ball to powder weight ratio of 5:2). In Al-CNTs composites powder milling, acetone was used as a process control agent (PCA) to prevent the melting of the material or preventing it from sticking to the balls and walls of the jar, and 0.08 % polyacrylic acid (PAA) was used as a dispersive agent. The milling time for Al-CNT composites was 20 hours at 200 rpm.

Milling operation was also performed to homogeneously mix reinforcement material SiC and Fe-based metallic glass with different weight percentages (5, 10, and 20) in Al matrix. The aim was to achieve good dispersion/distribution of reinforcements in the aluminum matrix. The milling time for Al-BMG and Al-SiC were 30 minute at 500 rpm.

2.2.2 Spark Plasma Sintering

The spark plasma sintering machine (model SPS 10-3), manufactured by Thermal Technologies LLC, was used to process aluminum matrix composites samples. As shown in Fig. 2.1, the SPS equipment consists of 3 main parts: power unit, heating furnace, and cooling and vacuum pumps. The direct current of 3000 amps and a potential of 5 V can generate a temperature of 2500 °C in less than 5 minutes. It is capable of attaining very high heating rates like 600 °C/min. A high cooling rate inside the furnace can be obtained by purging liquid nitrogen or liquid argon gas into it. To maintain the

purity of the samples, a high vacuum of 0.002 to 0.003 Torr can be attained during the sintering process. SPS equipment is provided with a hydraulic pump which can go up to 100 kN. Graphite dies and punches are used to fabricate samples at low pressures (≤100 MPa). K type and C type thermocouples are used to measure the die temperature during experiments.

Compaction of materials using SPS is mainly achieved by placing materials in between dies and punches at a required pressure and temperature. Selection and design of dies, punches, and spacers depends upon the temperature and pressure to be achieved. The sintering of aluminum matrix composites is considered low temperature and low pressure sintering as the melting point of aluminum is ~ 660 °C. The most widely used material for making dies and punches for spark plasma sintering is graphite due to its ease of availability, machining, and higher thermal and electrical conductivity at high temperatures. Graphite dies and punches are used to sinter aluminum matrix composites materials but not above 40 MPa of pressure.

Fig. 2.2 shows a position of a thermocouple inside the punch in the SPS setup. Instead of placing the thermocouple inside the die, it is placed in the lower punch through the spacer. Placing the thermocouple at this position measures a more accurate temperature without any effect of convection and radiation.

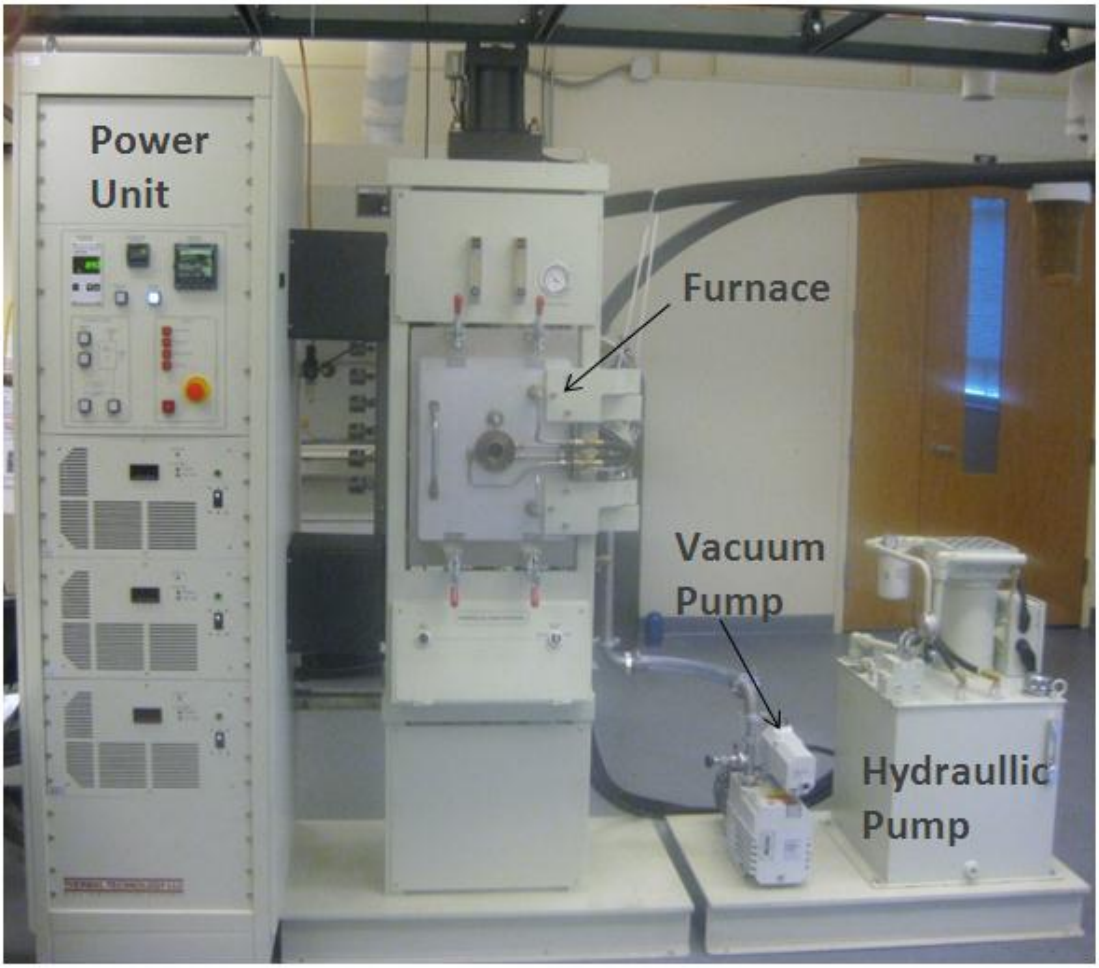

Fig. 2.1 Different components of spark plasma sintering equipment in the OSU laboratory

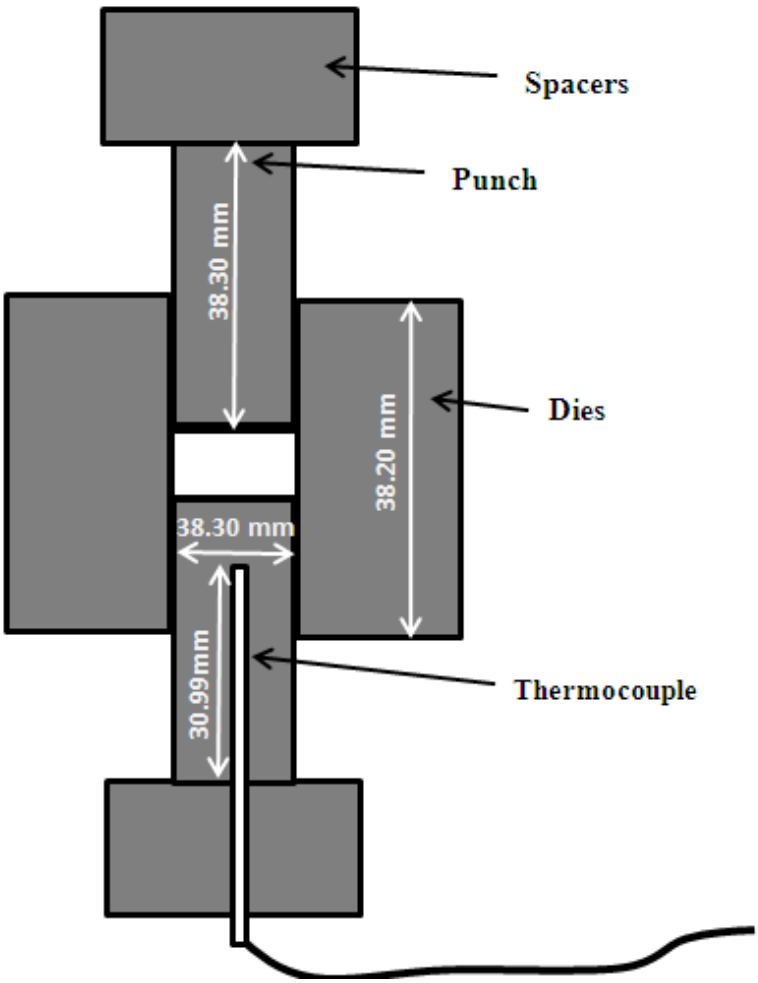

Fig. 2.2 The position of the thermocouple inside the graphite die and punch inside the SPS setup

2.3 Processing of Aluminum and Al-Matrix Composites

2.3.1 Fabrication of Bulk Samples of Aluminum and its Composites

Aluminum and Al-matrix composites (Al-CNT, Al-SiC, and Al-MG) are fabricated using spark plasma sintering. Samples are prepared of two different diameters, 20 mm and 10 mm, using dies and punches of graphite. Aluminum and Al-matrix composites are fabricated at 600 °C temperature and a pressure of 40 MPa with heating and cooling rate

of 100 °C/min. The thermocouple inserted into the bottom punch is used to measure the temperature. All the samples are fabricated in a closed furnace where 10^{-2} torr vacuum is maintained throughout the experiment.

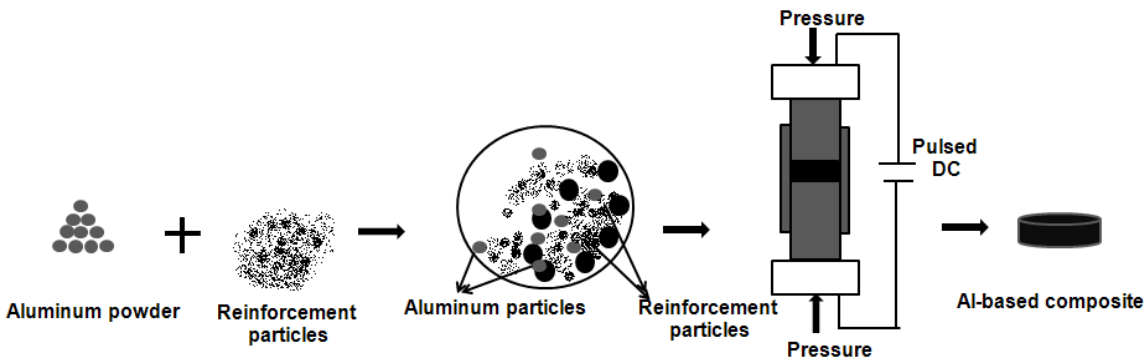

Fig. 2.3 The schematic of fabrication of Al-matrix composites using ball mill and spark plasma sintering

2.4 Characterization and Testing Methods

2.4.1 Density Measurement

Relative density measurement of aluminum and Al-matrix composites samples is carried out using Archimedes principle. Using this principle, relative density can be measured using the following equation.

$$\rho = \frac{x}{x-y}(\rho_0 - \rho_L) + \rho_L \quad \text{.....(2.1)}$$

Here,

ρ = Density of sample

x = Weight of sample in air

y = Weight of sample

ρ_o= Density of auxiliary liquid

ρ_L= Air density (0.0012 g/cm^3)

Theoretical density of aluminum: 2.7 g/cm^3

Density of water at 20 ºC: 0.99804

$$percentage of densification = \frac{Density of sintered sample}{Theoretical density of powder} \times 100 \ldots\ldots\ldots\ldots\ldots (2.2)$$

The density determination kit provided by Mettler Toledo is used for measuring the relative density of the samples.

2.4.2 Micro Structural and Phase Analysis

The x-ray diffraction (XRD) analysis of the spark plasma sintered aluminum bulk samples and Al-matrix composites was carried out using Philips Norelco x-ray diffractometer operating with Cu Kα (λ = 1.54178 Å) radiation at 45 kV and 40 mA. The diffraction angle was varied between 30º and 70º 2θ at a step increment of 0.02º 2θ with a count time of 1 s.

The characterization of the microstructure in the sintered discs was conducted using a SEM (JSM-6360, JEOL). The chemical characterization of the constituents in the aluminum matrix composite was conducted using energy dispersive spectroscopy (EDS). FEI Quanta 600 field-emission gun Environmental SEM with an Evex EDS X-ray microanalysis system and HKL EBSD system is used for EDS analysis.

2.4.3 Wear Test

The wear tests were performed on the spark plasma sintered aluminum samples and Al-matrix composite samples using a ball-on-disc tribometer under dry/unlubricated conditions (Nanovea Inc., Irvine, CA). The counterbody was an alumina ball with a

diameter of 6 mm. The wear tests were conducted using a normal force of 1 and 4 N and sliding velocity of 150 rpm on a 4 mm diameter track. The weight loss was recorded as a function of linear sliding distance. The sample surfaces before and after wear were analyzed using a SEM equipped with an energy dispersive spectroscopy (EDS) detector. Both topographic and back scattered images were used for analysis. The profiles across the wear track of samples were obtained using an optical surface profilometer (Nanovea Inc.).

2.4.4 Mechanical Testing

2.4.4.1 Microhardness Testing

A microhardness tester (Buehler Inc.) was used for measuring hardness by performing indentations at a load of 10 g and holding time of 10 s. The microhardness was measured on the polished surfaces of spark plasma sintered Al and Al-matrix composites. Around ten microhardness readings were taken at each location, and an average value with standard deviation are reported.

2.4.4.2 Nanoindentation Testing

Nanoindentation tests (Hystrion Inc.) were carried out on both aluminum and Al-CNT composite samples using a Berkovich indenter having 100 nm tip radius. The indentations were performed at loads of 100 μN and 200 μN with a loading rate of 10μN/s. At least five readings for nano-hardness were taken for each sample, and the average values with standard deviation are reported.

2.4.4.3 Compression Testing

Compression testing was performed on spark plasma sintered cylindrical samples of aluminum and the Al-CNT composite (length to diameter ratio of 1), which is obtained by quasi-static mechanical loading using INSTRON 5582series Universal testing machines. A strain rate of 10^{-4} s^{-1} is used in order to ensure the quasi-static nature of the experiment.

CHAPTER 3

RESULTS AND DISCUSSION

3.1 Spark Plasma Sintering of CNT Reinforced Aluminum Composites

3.1.1 Microstructure Characterization Al-CNT composites

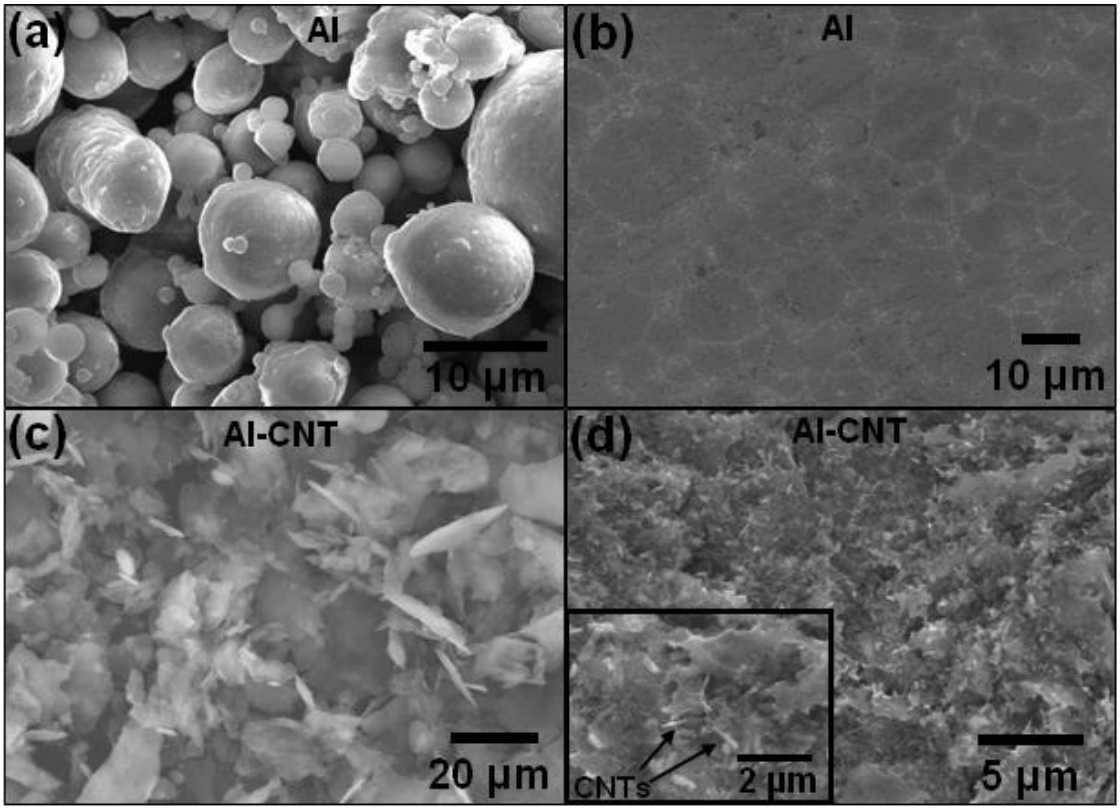

Fig. 3.1 SEM images from (a) starting aluminum powder, (b) spark plasma sintered aluminum, (c) ball milled Al-CNT powder mixture, and (d) spark plasma sintered Al-CNT composites

Microstructures of starting aluminum powder and spark plasma sintered aluminum are presented in Fig. 3.1 (a-b). The starting aluminum consisted of spherical particles over a wide range of particle size (<40 μm). With the SPS processing parameters investigated in this work, near complete densification (~100% relative density) of aluminum was observed. It can be observed that the grains in the sintered aluminum samples were fairly spherical with some faceted boundaries due to deformation during SPS sintering. The grain size and distribution are not significantly different than that for starting powder suggesting full densification without significant grain growth during sintering.

SEM images from the ball milled powder Al-CNT mixture and spark plasma sintered bulk composite discs are also presented in Fig. 3.1 (c-d). The figure shows deformed plates of aluminum embedded with CNTs in the balled milled powder. The SPS resulted in near complete densification of Al-CNT composite with fairly uniform dispersion of CNTs in the aluminum matrix. The relative density of Al-CNT composites (~98.6%) was slightly lower than that for aluminum processed with similar SPS processing parameters indicating that CNTs restrict the densification of composite. Similar effect of CNTs on restricting the densification was observed for Al-CNT composites processed using isostatic pressing followed by hot extrusion [14]. The CNTs protruding out of the aluminum matrix can be clearly seen in the microstructures (inset of Fig. 3.1(d)). It seems that PAA random coils tend to adsorb on the sidewalls or within the ends of the CNTs resulting in better dispersion of the CNTs in the aluminum matrix composites. Such mechanisms of CNT dispersion using PAA dispersant have been previously demonstrated by Tran *et al.* using detailed transmission electron microscopy (TEM) and near edge x-ray adsorption fine structure spectroscopy (NEXAFS) [80].

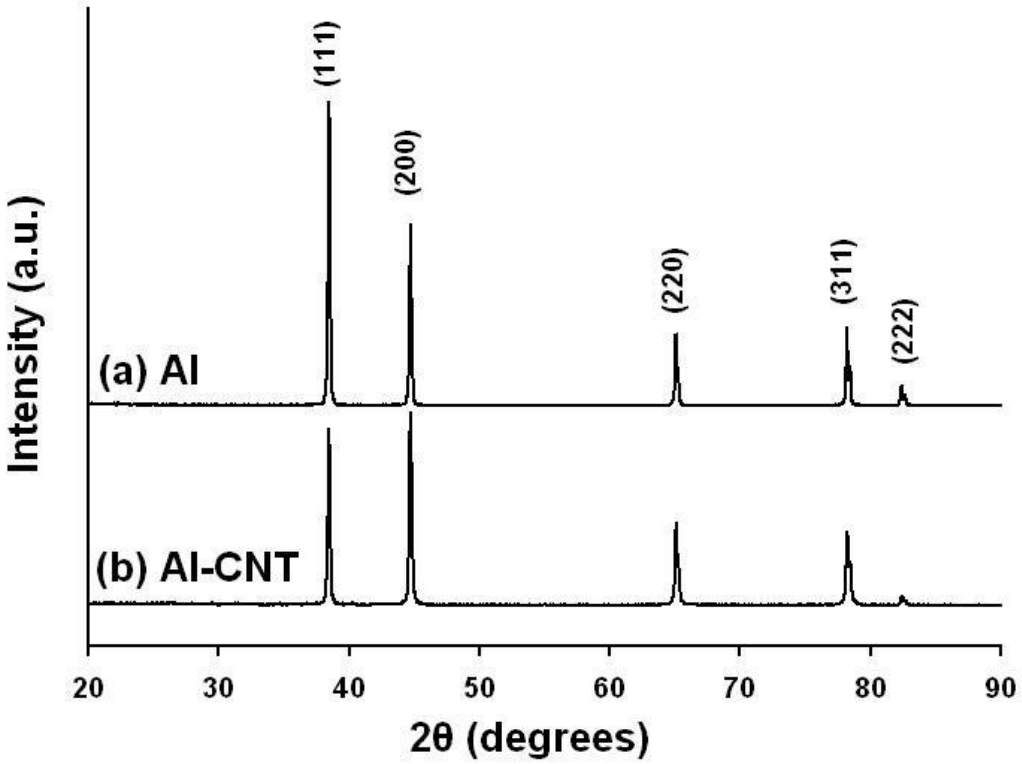

Fig. 3.2 X-ray diffraction patterns from spark plasma sintered (a) aluminum, and (b) Al-CNT composites

X-ray diffraction (XRD) patterns from the spark plasma sintered aluminum and Al-CNT composites are presented in Fig. 3.2. As can be expected, both the XRD patterns showed primary aluminum peaks. Note that characteristic (002) peak (2θ=26.2°) corresponding to CNTs could not be found in the XRD pattern from the Al-CNT composite. This could be due to very low content and fairly uniform distribution of CNTs in the aluminum matrix. Similar observations have been made for cold compacted and hot extruded Al-2 wt.% CNT composites [71]. Furthermore, no peaks corresponding to aluminum carbide (Al_4C_3) appeared in the XRD pattern indicating that there was no undesirable interfacial reaction between aluminum matrix and CNT reinforcement during

SPS sintering. The formation of such carbides is often found in case of conventional processing of Al-CNT composites [81]. The rapid SPS processing at relatively lower temperature seems to avert such undesirable interfacial reactions in Al-CNT composites.

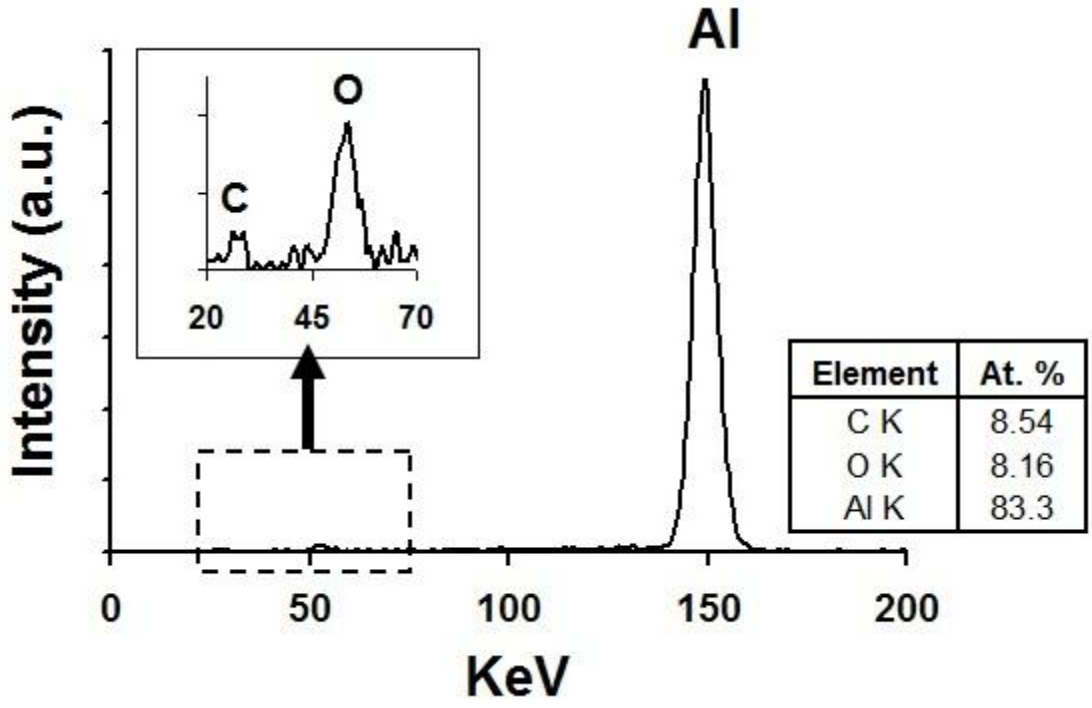

Fig. 3.3 EDS spectrum and corresponding elemental composition of Al-CNT composites

To get further insight into compositional changes associated with SPS sintering of Al-CNT composites, EDS analysis of the composite was conducted (Fig. 3.3). In addition to an intense aluminum peak, the EDS spectrum also showed minor peaks corresponding to carbon and oxygen. The quantitative analysis from EDS spectrum showed oxygen content of about 8.2 at.% in the composite. The presence of oxygen peak could be due to surface oxidation of the starting aluminum powder. Note that presence of aluminum oxides could not be resolved using XRD analysis.

3.1.2 Micro- and Nano-Mechanical Testing:

The microhardness of Al-CNT composites (average hardness=88 HV (~0.86 GPa)) was found to be over two times that of aluminum (average hardness=36 HV (~0.35 GPa)) sintered with similar SPS parameters. The microhardness of the spark plasma sintered Al-CNT composites of this investigations is also higher than the previously reported hardness values for similar compositions of Al-CNT composites prepared by hot pressing and spark plasma sintering (~48-50 HV for Al-CNT composites with 0.5-2 wt.% of CNTs) [73].

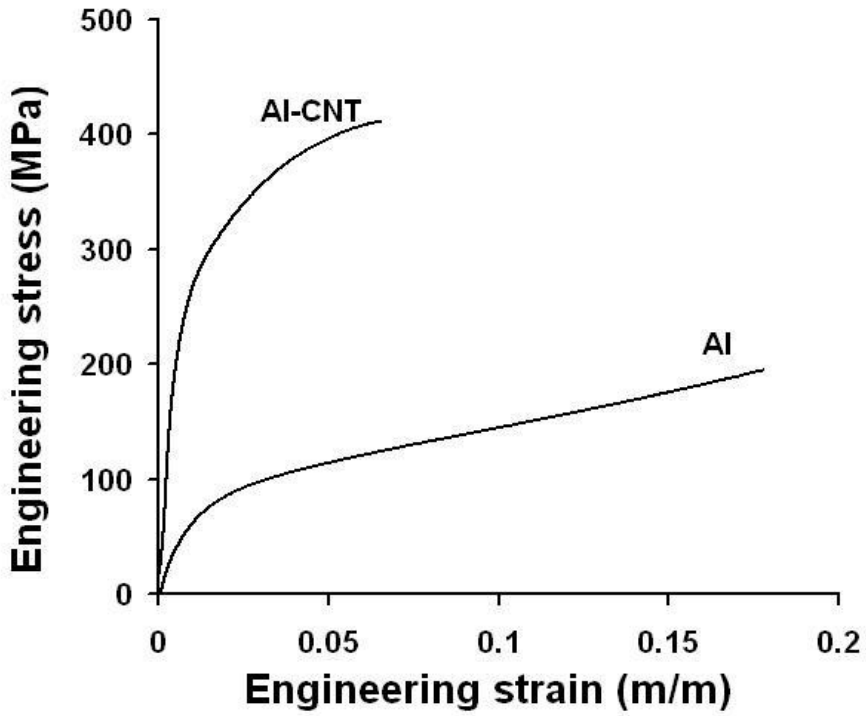

Fig. 3.4 Representative compressive stress-strain curves of spark plasma sintered aluminum and Al-CNT composites

The representative compressive stress-strain curves of spark plasma sintered aluminum and Al-CNT composites are presented in Fig. 3.4. Clearly, the addition of

CNTs resulted in significant improvement in the compressive yield strength of the composites ($\sigma_{YS,\ Al}$=80 MPa; $\sigma_{YS,\ Al\text{-}CNT}$=280 MPa). The compressive yield strength values observed in this work are significantly higher than previously reported values for Al-CNT composites fabricated using spark plasma sintering followed by hot extrusion ($\sigma_{YS,\ Al\text{-}CNT}$=86 MPa) [73]. The lower values of compressive strength of Al-CNT composites (with 2 wt.% CNTs) in this previous report was primarily due to clustering of CNTs in the extruded direction. Improved values of compressive strength in this work seem to be due to fairly uniform distribution of CNTs in the aluminum matrix. While dispersion strengthening effect is the commonly accepted mechanism for improvement in hardness of Al-CNT composites, some investigations have indicated that CNTs also restrict the aluminum grain growth during thermal processing resulting in grain boundary strengthening. The grain boundary strengthening effect due to addition of CNTs was demonstrated in Al-CNT composites fabricated using isostatic pressing followed by hot extrusion [14]. Due to relatively shorter sintering time and lower sintering temperature with the SPS processing, significant grain growth effects are not expected. Nevertheless, high resolution transmission electron microscopy (TEM) studies are required to clearly delineate the dispersion strengthening and grain boundary strengthening effects. These detailed investigations are currently underway, and the results of these studies will be presented in separate focused article.

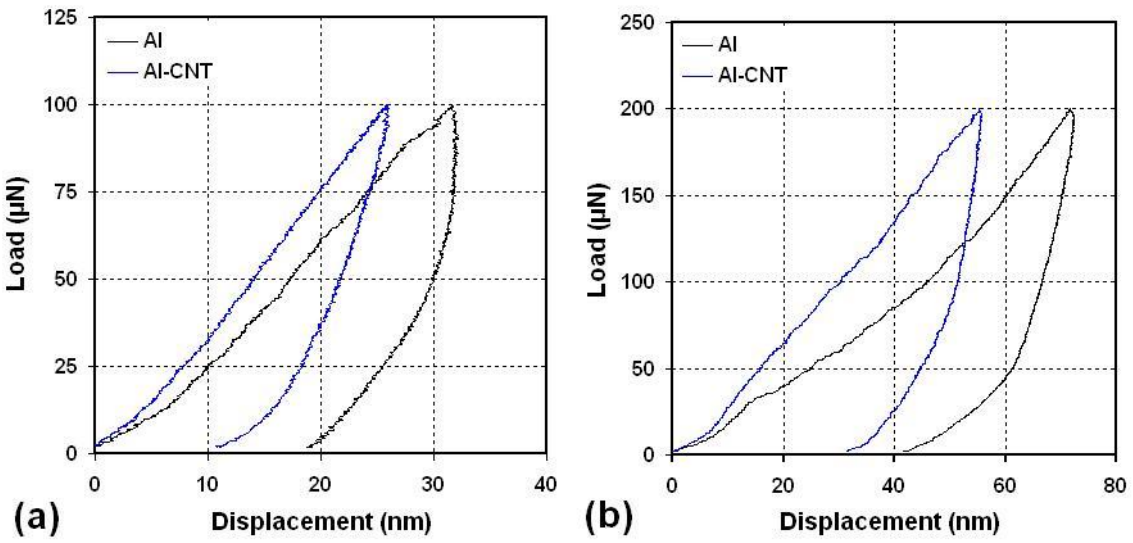

Fig. 3.5 Typical nanoindentation load-displacement curves for aluminum and Al-CNT composites obtained with peak loads of (a) 100 μN, and (b) 200 μN

Typical nanoindentation load-displacement curves for aluminum and Al-CNT composites with two different peaks loads (100 and 200 μN) are presented in Fig. 3.5. The average values of elastic modulus for aluminum and Al-CNT composites were 65±4 GPa and 84±3 GPa, respectively. Also, the average values of nanohardness for aluminum and Al-CNT composites were 0.95 (±0.12) GPa and 1.42 (±0.20) GPa, respectively. Clearly, the reinforcement of 2 wt.% CNTs in aluminum resulted in about 29% and 50% increase in the elastic modulus and nanohardness, respectively. Increasing modulus and nanohardness indicate strengthening and stiffening effects associated with the reinforcement of CNTs in aluminum matrix. It can be seen that nanohardness values for both the samples are significantly higher (about 1.5 to 3 times) than microhardness values. This could be due to highly localized nature of the nanoindentation method where the hardness is influenced by the features or effects in a very small volume of test

material. Similar differences in hardness values obtained with nanoindentation and microindentation have been reported earlier for thermal spray Al-CNT coatings [62]. It is well known that nanoindentation values of ductile materials are very sensitive to the material pile-ups around the hardness impression [82]. To further investigate the material pile-ups, nanoindentation tests were conducted with higher peak load (9000 μN). Typical images of the nanoindentation impressions and corresponding depth profiles across the images for aluminum and Al-CNT composites are shown in Fig. 3.6. The size and depth of the impression for Al-CNT composite were significantly smaller than that for aluminum indicating the strengthening effect of CNTs. For both the samples, the material pile-up was relatively larger at the edge than at the corner of the indent impressions. In general, significant pile-up results in the overestimation of the hardness and modulus values obtained using Oliver and Pharr procedure [83]. The parameter h_f/h_{max} (h_f and h_{max} are displacements at peak load and after complete unloading, respectively) is often taken as an indicator of the amount of pile-up. For accurate nanoindentation results using Oliver and Pharr procedure, the h_f/h_{max} should be less than 0.7. In all of our nanoindentation data, the h_f/h_{max} ratio was less than 0.7 (average 0.61 for aluminum and 0.54 for Al-CNT composites).

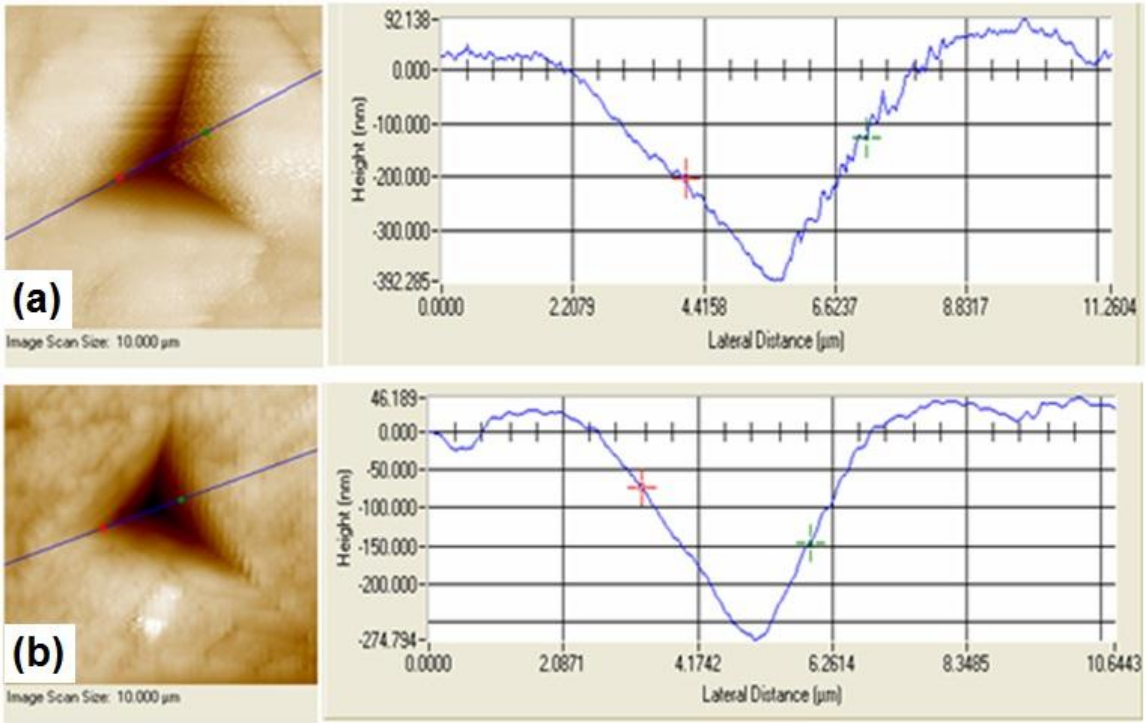

Fig. 3.6 Typical images of nanoindentation impressions and associated depth profiles for (a) aluminum, and (b) Al-CNT composites (nanoindentation peak load of 9000 μN)

3.1.3 Wear Characteristics

Fig. 3.7 presents the cumulative weight loss as a function of sliding time for aluminum and Al-CNT composites during ball-on-disc wear testing conducted with normal force of 1N.

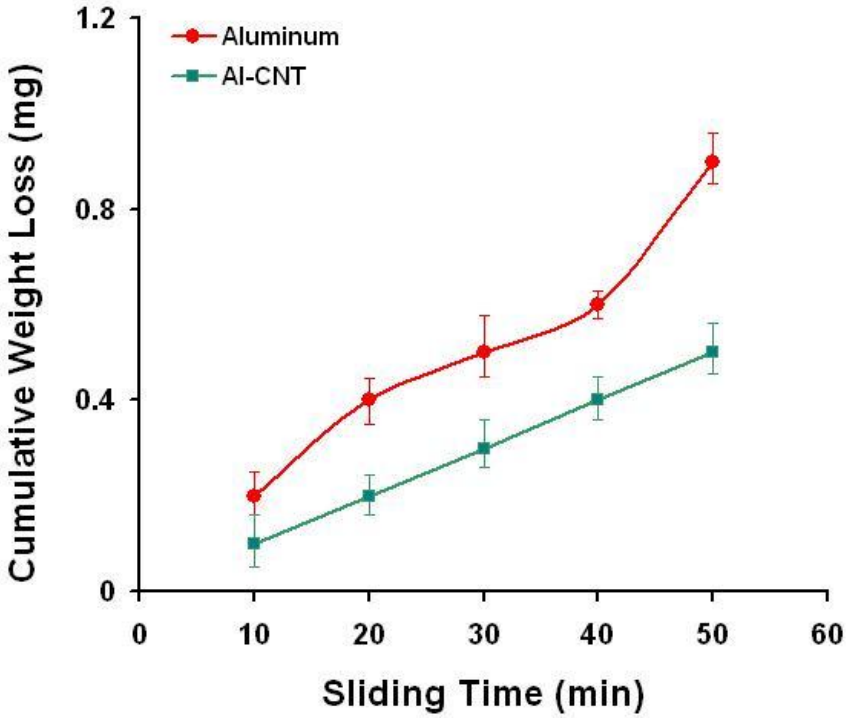

Fig. 3.7 Cumulative weight loss as a function of sliding time during ball-on-disc wear testing conducted with normal force of 1N for aluminum and Al-CNT composites

While the Al-CNT composites exhibited lower and fairly linear wear rate (slope of the weight loss-time curve), the aluminum samples showed accelerated wear in early and later stages of wear test. For all the time intervals, the cumulative wear weight loss for Al-CNT composites was relatively lesser than that for aluminum. The reduction in total wear weight loss due to CNT reinforcement in the Al-CNT composites was about 45%, suggesting significantly improved wear resistance of the composites.

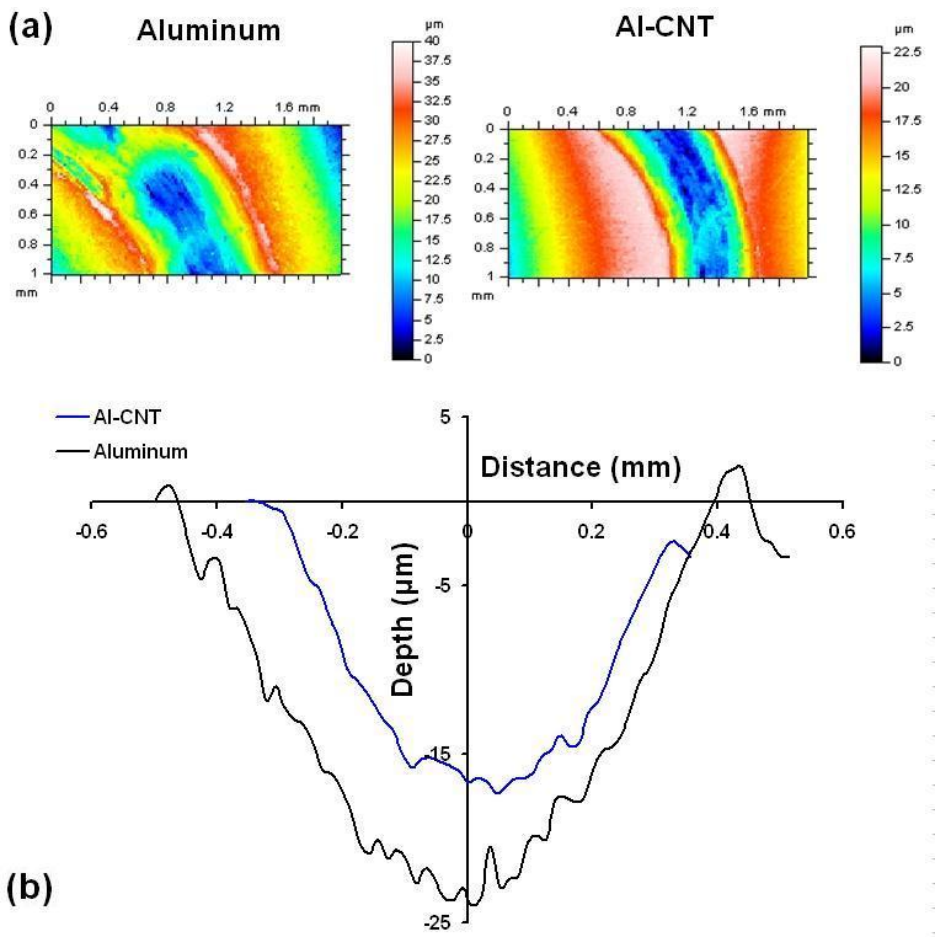

Fig. 3.8 (a) surface profiles of wear tracks, and (b) line profiles across the wear tracks for aluminum and Al-CNT composites

The depth profiles across the wear tracks after complete wear testing for aluminum and Al-CNT composites are also shown in Fig. 3.8. The reinforcement of CNTs resulted in about 30% reduction in depth and width of the wear track for Al-CNT composites. The depth profile also shows some material pile-up (~2 µm high) at the edges of the aluminum wear track indicating plastic deformation. Such material pile-up at the edges of wear track was not significant for Al-CNT composites.

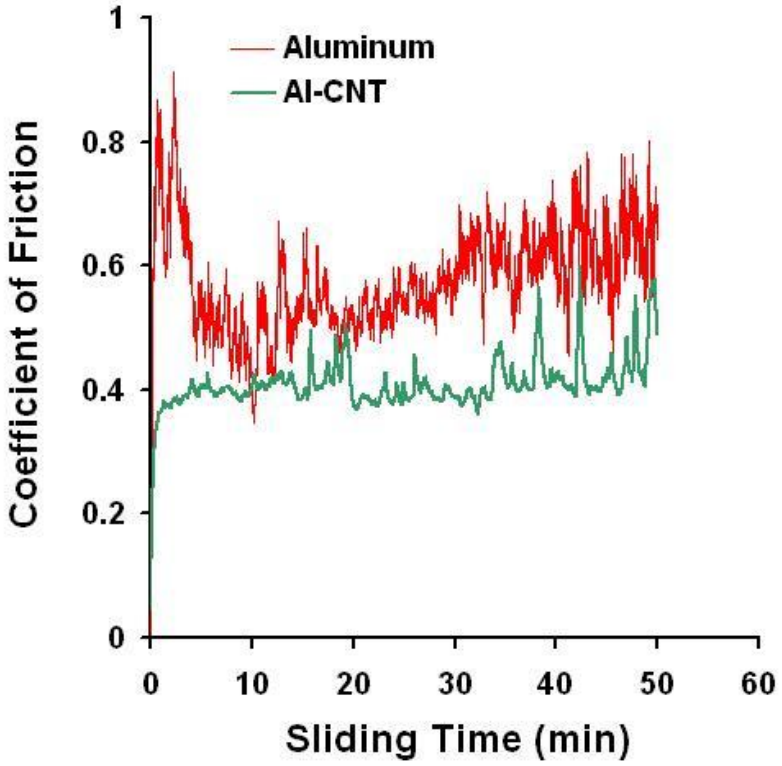

Fig. 3.9 Variation of coefficient of friction with sliding time during ball-on-disc wear testing conducted with normal force of 1N for aluminum and Al-CNT composites

The cumulative weight loss and wear depth/width data clearly indicate that Al-CNT composites exhibited improved wear resistance than aluminum. The variation of coefficient of friction with sliding time during wear tests for aluminum and Al-CNT composites is presented in Fig. 3.9. For aluminum samples, the variation of coefficient of friction was somewhat erratic with very high values (~0.65-0.85) in the initial stages (0-5 min) and relatively lower values (~0.45-0.65) in later stages (30-50 min) of the sliding wear test. For Al-CNT samples, the coefficient of friction rapidly increases to about 0.4 and remains fairly stable at that value for the rest of the test. Some fluctuations in the friction coefficient for Al-CNT samples can be seen, especially in the later stages of wear

test. The coefficient of friction for Al-CNT composites was relatively lower than that for aluminum samples.

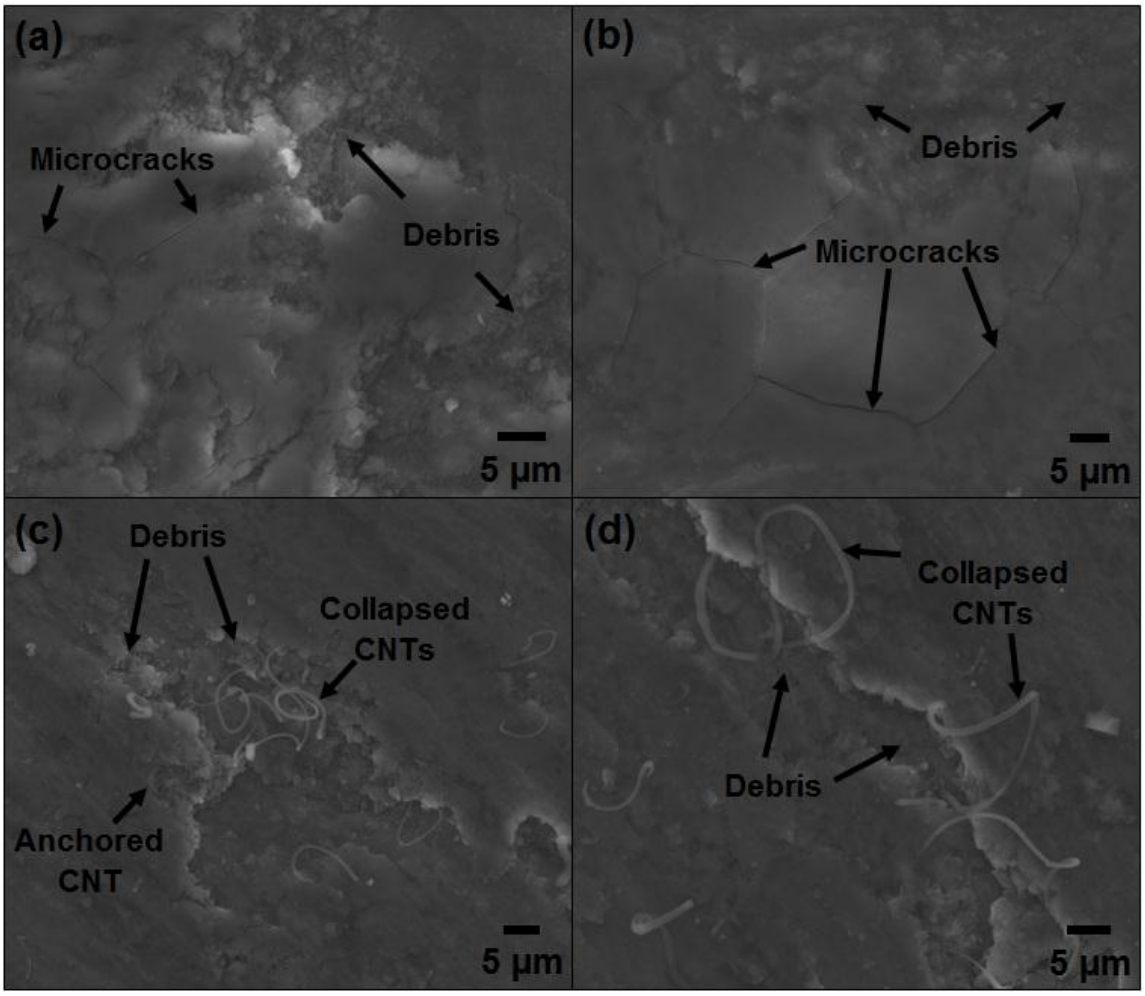

Fig. 3.10 SEM images from the worn surfaces of (a-b) aluminum, and (c-d) Al-CNT composites

SEM images from the surface of wear tracks for aluminum and Al-CNT composites are presented in Fig. 3.10. For worn surfaces of aluminum samples exhibit distinct smooth regions (load bearing) at higher elevation and rough regions (filled with fine debris) at lower elevation. Fine micro-cracks along the grain boundaries in the smoother regions can also be seen. It seems that such micro-cracks dislodge the grains leading to formation

of depressed regions (at lower elevation) which subsequently get filled with abrasive debris. The worn surfaces of the Al-CNT composites also show smooth regions and depressed regions. The smoother regions showed distinct scratch marks (parallel to sliding direction) characteristics of abrasive wear. The depressed regions of these worn surfaces were filled with abrasive debris and also the collapsed CNTs. The collapsed CNTs can also be seen on the smoother regions of the worn surface. No visible cracking on the worn surfaces of Al-CNT composites was observed. It seems that CNTs prevent cracking along the grain boundaries by anchoring smoother and depressed regions of the worn surface. The relatively lower coefficient of friction for Al-CNT samples can also be attributed to the distribution of self-lubricating CNTs on the worn surface. The CNTs on the worn surface seem to reduce direct contact between the surface and the counterbody resulting in improved wear resistance and lower friction coefficient for the composite samples [66].

3.2 Spark Plasma Sintering of SiC Reinforced Aluminum Composites

3.2.1 Microstructure Characterization of Al-SiC Composites

SEM images of spark plasma sintered Al-SiC bulk composites disc are presented in Fig. 3.11 (a-f). They show scratches formed on the surfaces, mainly produced by the rubbing of SiC particles that came out during polishing. This is because of weak interfacial bonding between Al and SiC. Fig. 3.12 shows the EDS of Al-SiC composites, which represents the uniform distribution of SiC particles in the aluminum metal matrix using ball milling. The relative density of Al-SiC composites was slightly lower than that for aluminum and decrease relatively, as the reinforcement content increase with similar SPS processing parameters (as shown in Fig. 3.13). Some porosity was observed, which might be due to the higher melting point (~2700 °C) of SiC reinforcement particles.

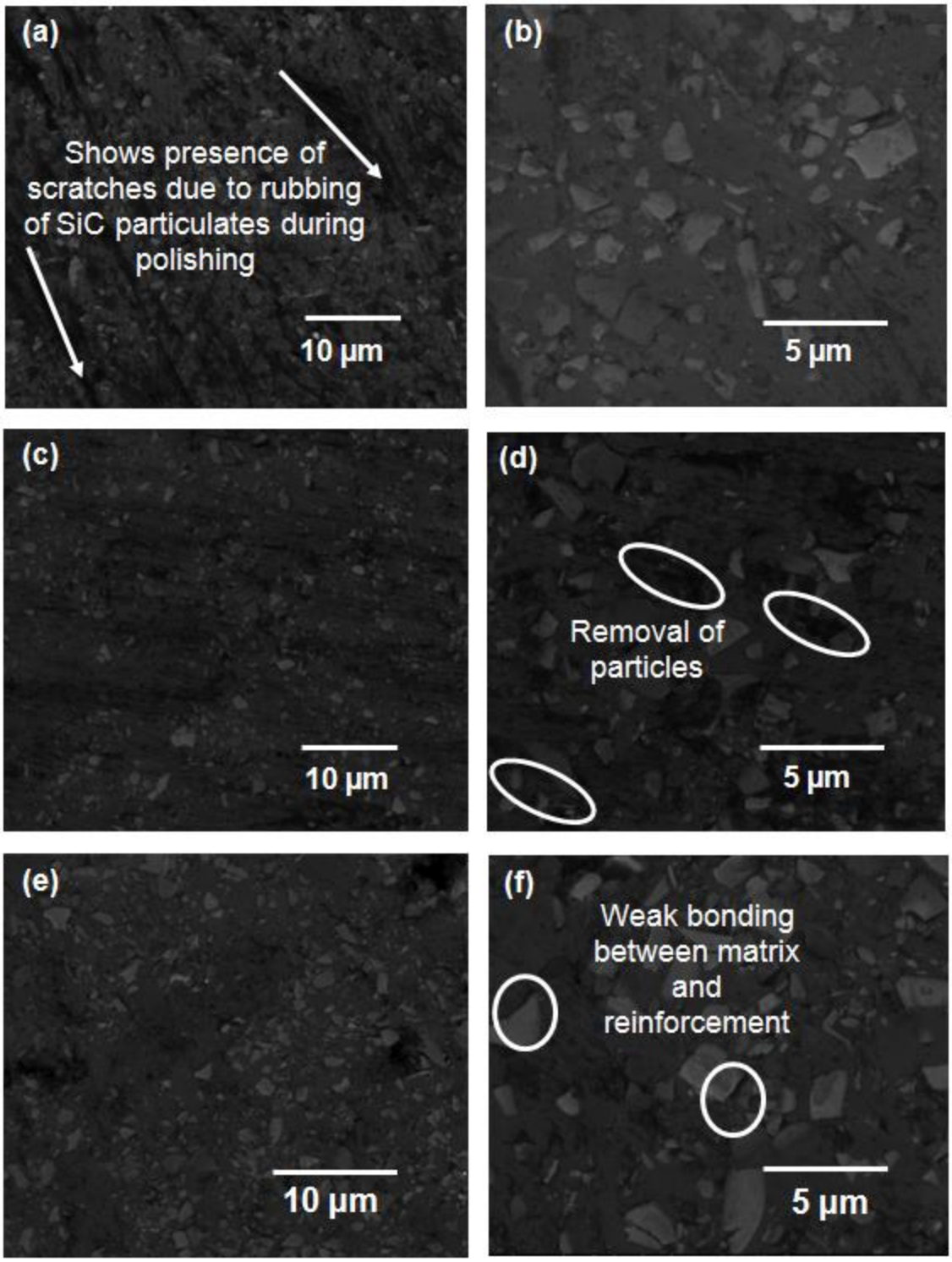

Fig. 3.11 SEM images of spark plasma sintered Al-SiC composites (a-b) 5 wt.% , (c-d) 10 wt.% ,and (e-f) 20 wt.% SiC

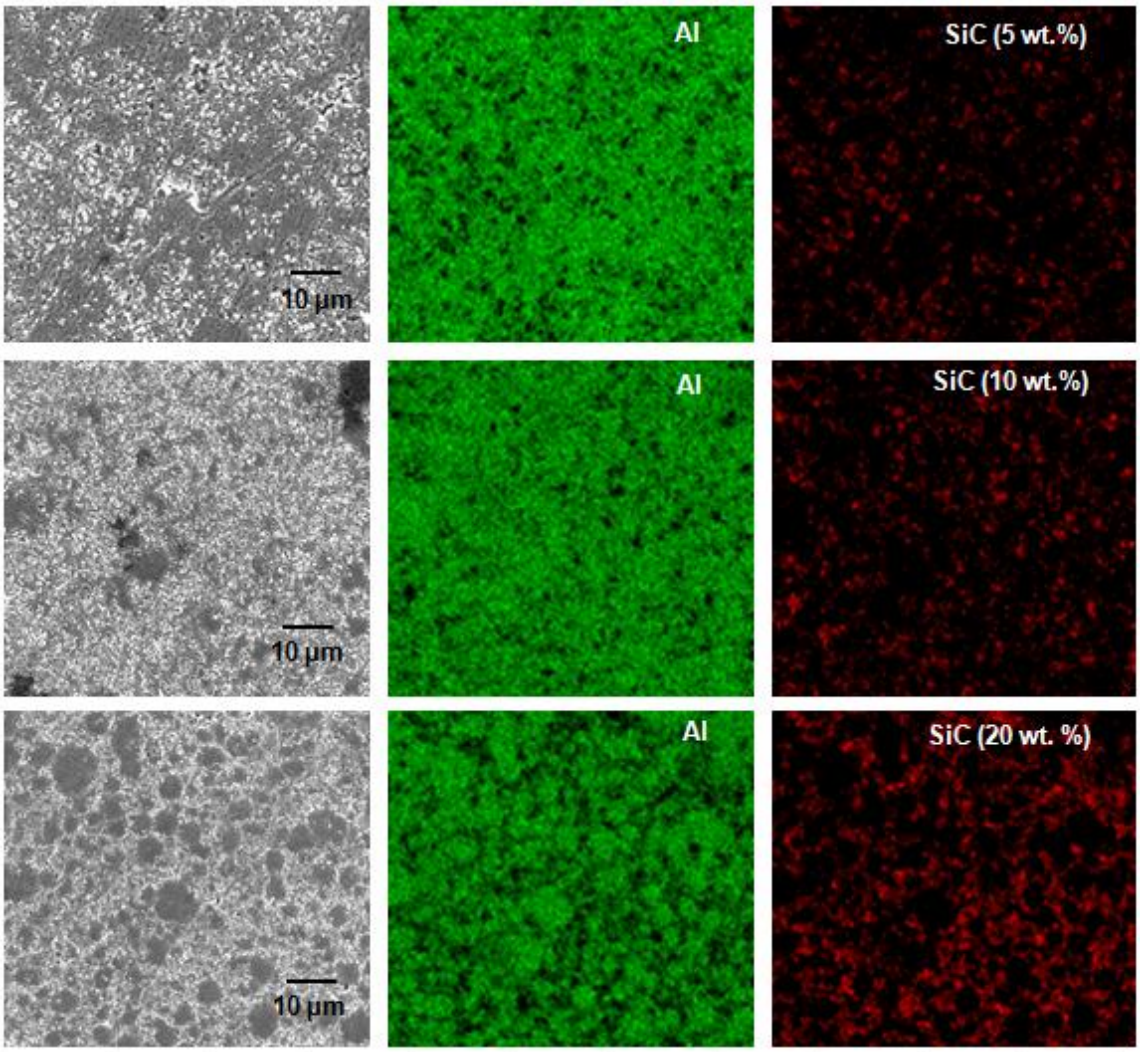

Fig. 3.12 EDS of Al-SiC composites with reinforcements of 5, 10, and 20 wt.% SiC

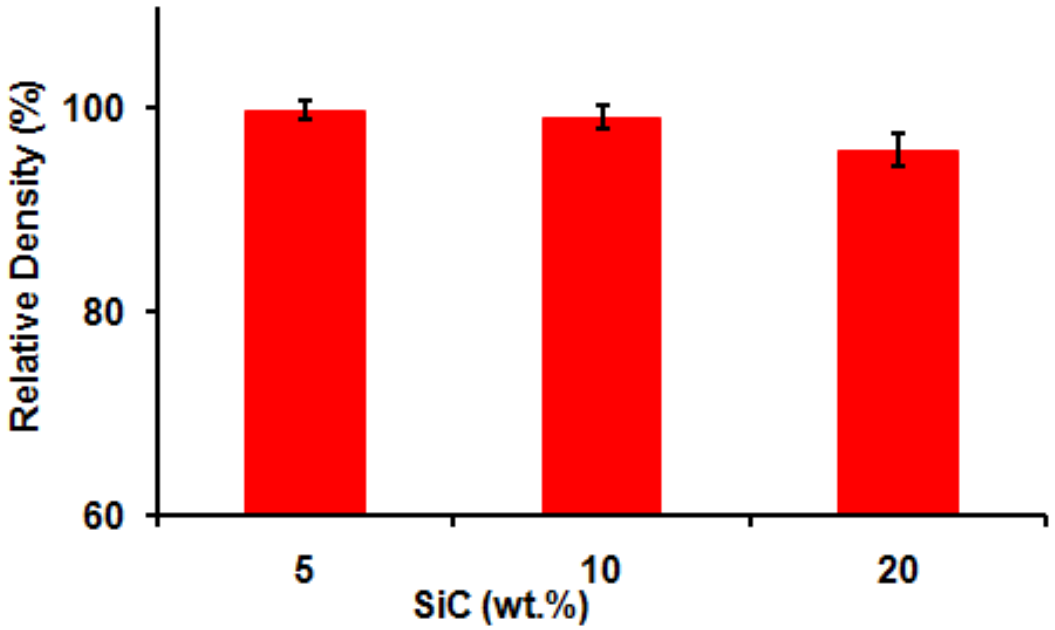

Fig. 3.13 Relative densities of Al-SiC composites with reinforcement of 5, 10, and 20 wt.% SiC

X-ray diffraction (XRD) patterns from the spark plasma sintered Al-SiC composites are presented in Fig. 3.14. All three XRD patterns showed primary aluminum peaks and corresponding SiC peaks at 37°, 60°, and 83° 2θ angles. However, intensity of Al peaks is relatively decreasing, as the content of reinforcement is increasing.

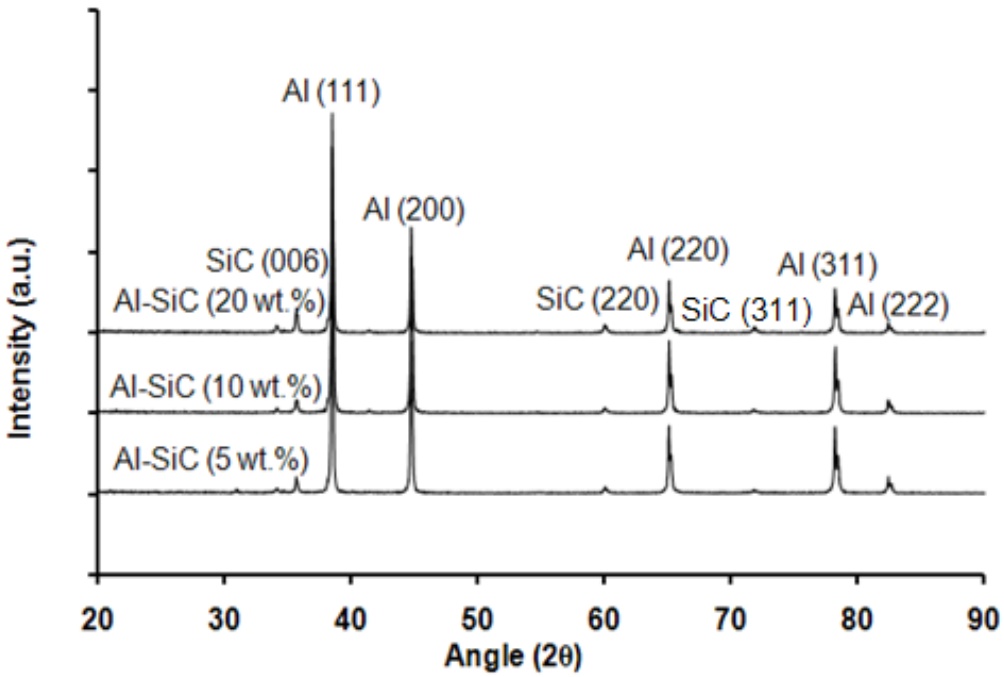

Fig. 3.14 X-ray diffraction patterns from spark plasma sintered Al-SiC composites with reinforcement of 5, 10, and 20 wt.% SiC

3.2.2 Microhardness

The average microhardness of Al-SiC composites with 5, 10, and 20 wt.% of SiC reinforcement were found to be 74 (±5), 77 (±5), and 87 (±6) HV, respectively (shown in Fig. 3.15). With the similar SPS processing parameters, the average microhardness of aluminum was found to be 36 (±4) HV. The microhardness of Al-SiC composites shows a significant increase in hardness of composites with the increase in the content of reinforcement.

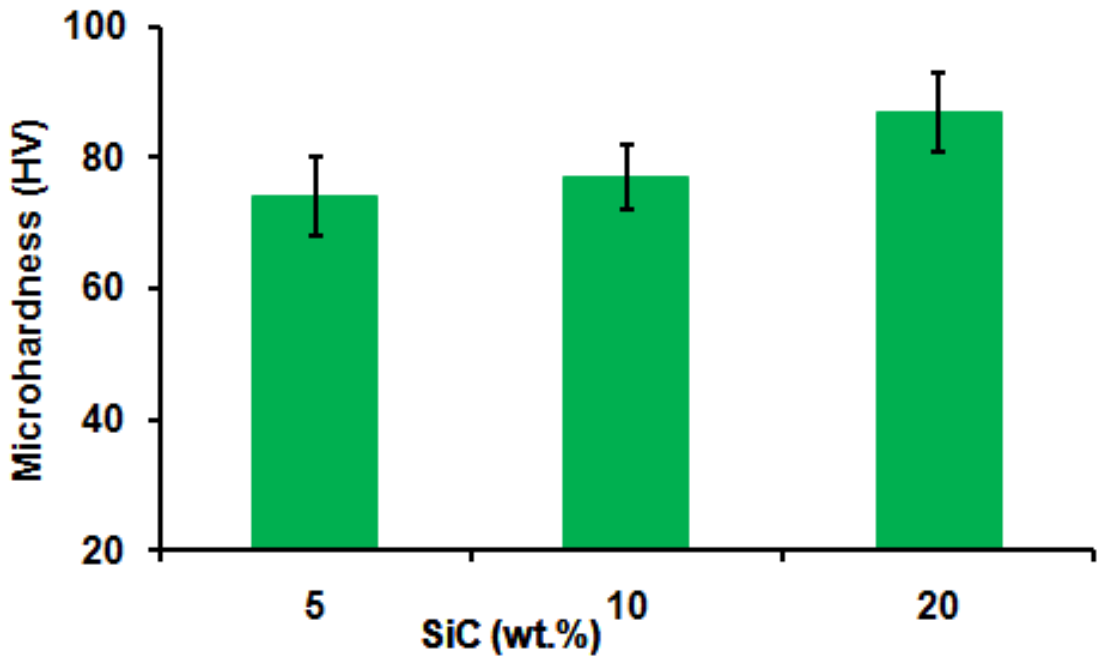

Fig. 3.15 Vickers microhardness of Al-SiC composites with reinforcement of 5, 10, and 20 wt.% SiC

3.2.3 Wear Characteristics

Fig. 3.16 represents weight loss as a function of sliding time for aluminum and Al-SiC composites during ball-on-disc wear testing conducted with a normal force of 4N. The Al-sample exhibits a higher wear weight loss, while the Al-SiC composites show a lower wear weight loss. As observed from this data, weight loss decreased by around 2.2 times by reinforcing aluminum with 5 wt.% SiC. Similarly, when compared to aluminum, decrease in weight loss was 3 times for 10 wt.% and 2 times for 10 and 20 wt.% reinforced SiC. The reduction in wear weight loss for Al-SiC with 10 and 20 wt.% composites are almost same. It might be due to the higher content of reinforcement particles. The weight loss data clearly indicates that the Al-SiC composites exhibited improve wear resistance more than aluminum. Therefore, it shows SiC as an effective

reinforcement for increasing the wear resistance of aluminum. Significant improvement in microhardness was also observed by reinforcing aluminum with SiC.

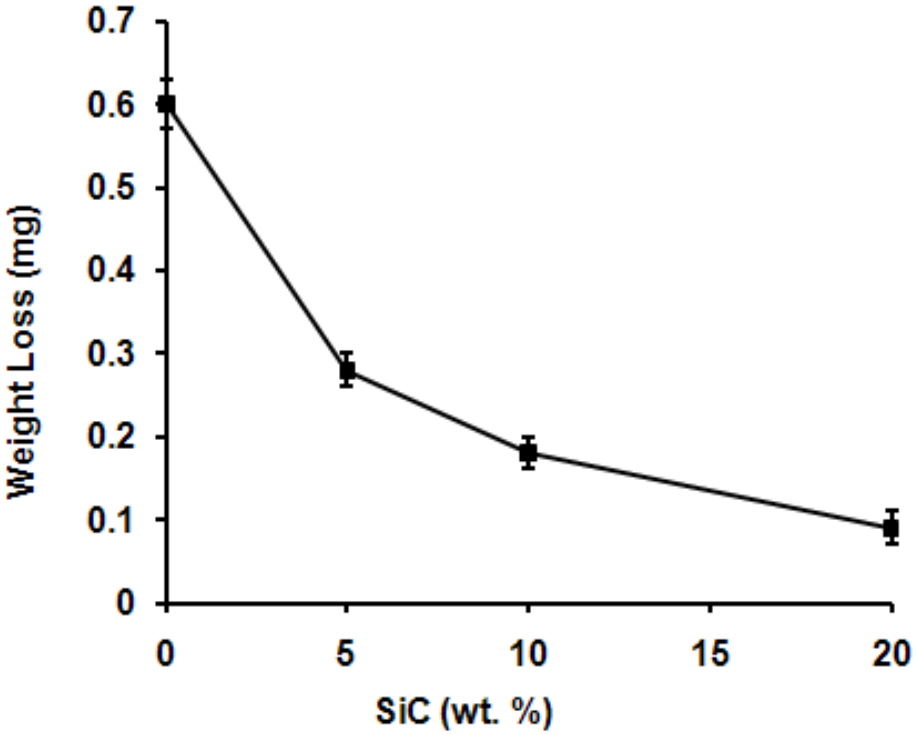

Fig. 3.16 Weight loss as a function of sliding time during ball-on-disc wear testing conducted with normal force of 4 N for aluminum and Al-SiC composites

The variation in coefficient of friction for aluminum and Al-SiC composites with reinforcement content of 5, 10, and 20 wt.% is presented in Fig. 3.17. For the aluminum sample, the variation of coefficient of friction was somewhat inconsistent with high values (~0.2-0.8) in the initial stage (0-2 min) and relatively lower values (~0.6-0.66) in the later stages (2-10 min) of the sliding wear test. For Al-SiC composites sample, the coefficient of friction for 5 and 10 wt.% SiC reinforcement aluminum composites lies between 0.5 to 0.9 and 0.5 to 0.65, respectively. Some fluctuation can be seen in Al-SiC

composites, especially in the case of Al-5wt.% SiC composite. However, the average coefficient of friction for Al-20 wt.% SiC composite is around 0.45, which is relatively less.

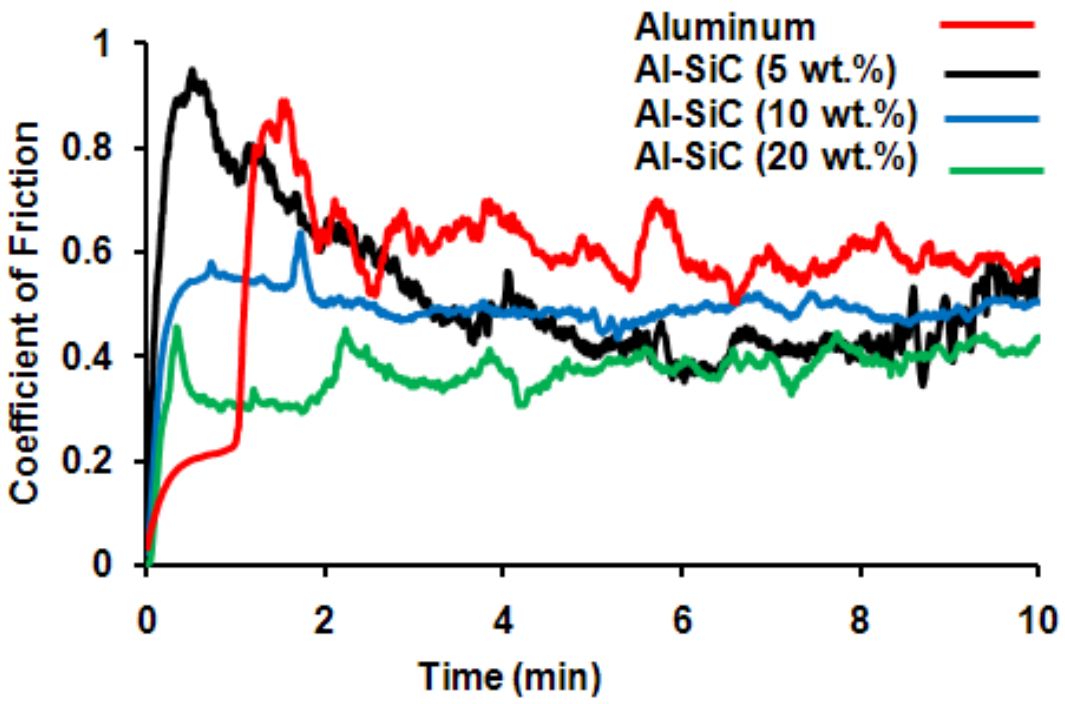

Fig. 3.17 The coefficient of friction with sliding time (10 min) during ball-on-disc wear testing conducted with normal force of 4 N for aluminum and Al-SiC composites

Fig. 3.18 shows a profile of the wear track for Al-SiC composites. The wear profile data matches well with the wear loss data. There is a significant difference between the heights and widths of the wear tracks, which accounts for less wear loss as the content of SiC is increasing. Therefore, Al-20 wt.% SiC composite shows low wear loss.

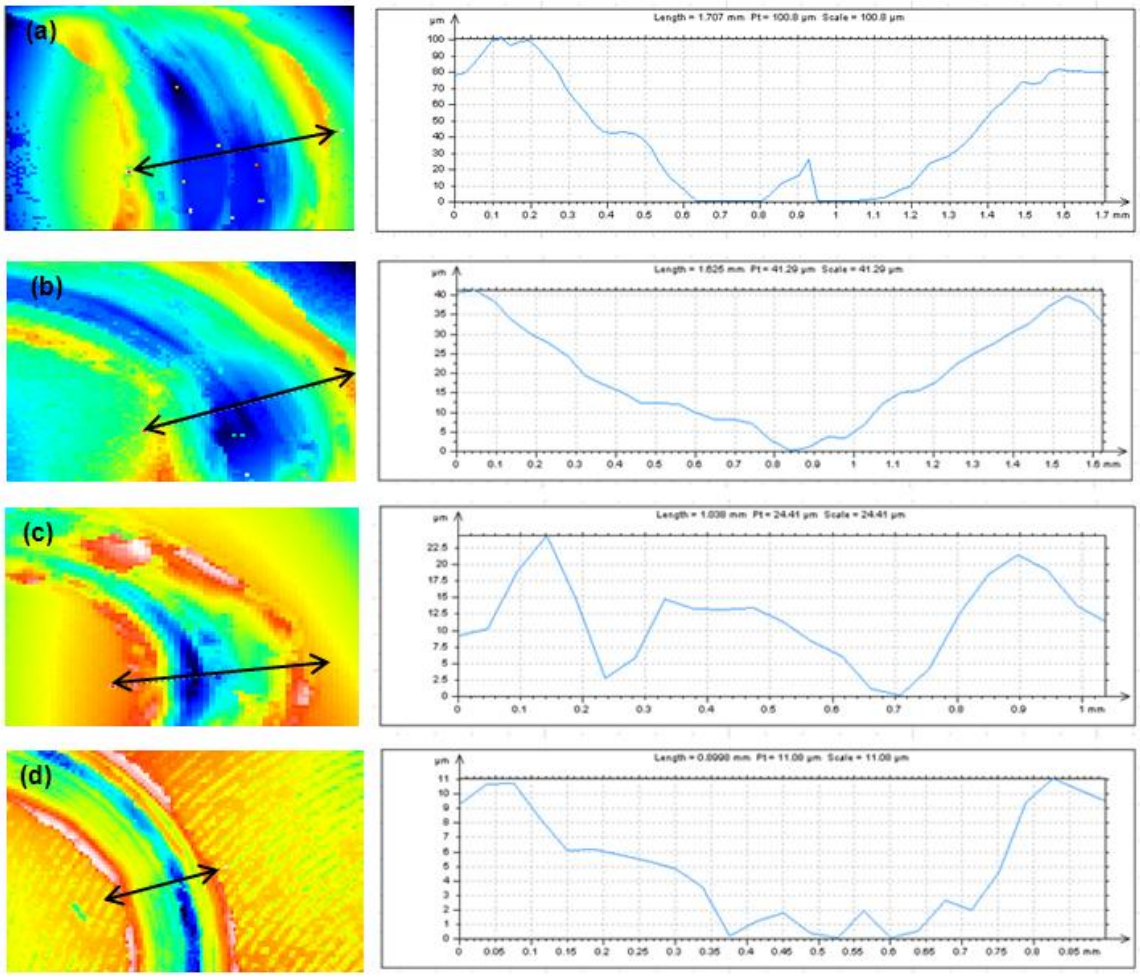

Fig. 3.18 Surface profiles of wear tracks of Al-SiC composites (a) pure aluminum (b) 5wt%, (c) 10 wt.%, and (d) 20 wt.% SiC

To further investigate the wear mechanism of SiC reinforced Al-composites, SEM images of the wear track were collected and analyzed. Wear surface of the SiC reinforced Al matrix is shown in the Fig. 3.19. Presence of microcuts is mainly due to abrasion caused by Al_2O_3 balls on the composite surface. Existence of deep grooves is mainly due to dislodging of SiC particles during later stage of wear. These removed SiC particles

also act as microchips which can further abrade the matrix and cause increase in weight loss.

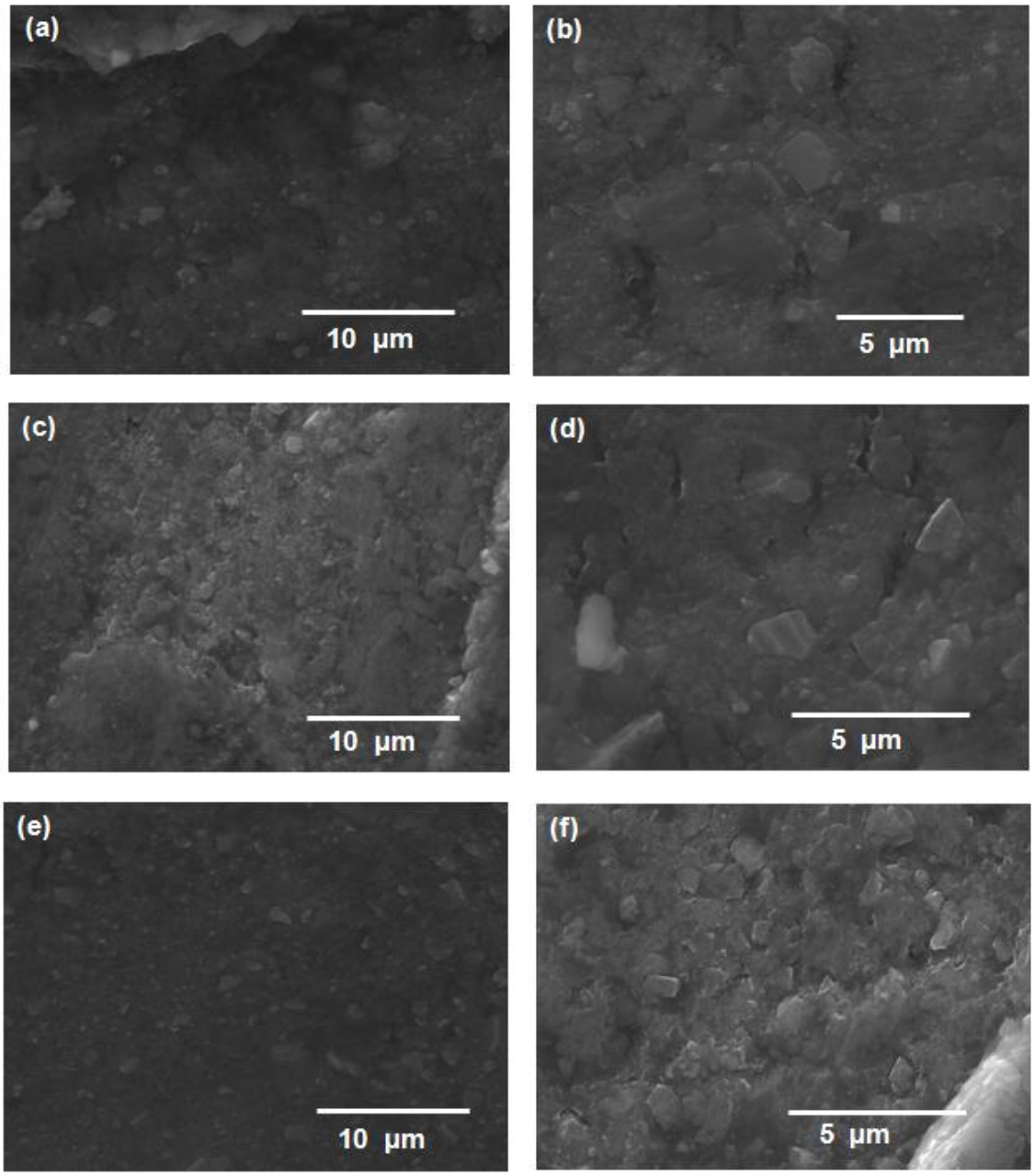

Fig. 3.19 SEM images wear track of spark plasma sintered Al-SiC composites (a-b) 5 wt.% , (c-d) 10 wt.% , and (e-f) 20 wt.% SiC

3.3 Spark Plasma Sintering of Iron-based Metallic Glass (MG) Reinforced Aluminum Composites

3.3.1 Microstructure Characterization of Al-MG Composites

Metallic glasses are a new class of materials, having superior properties like high hardness, strength, wear, and corrosion resistance. A lot of emphasis is given on the development of bulk metallic glasses and its composites; however, not many studies were made on using metallic glasses as reinforcements. In this study, we have used Fe-based metallic glass having composition of 5, 10, and 20 wt.% as reinforcement for pure aluminum powder.

As it is discussed in an earlier section, the starting aluminum powder and sintered aluminum consisted of spherical particles over a wide range of particle size of less than 40 µm, as shown in Fig. 3.1 (a-b). Nearly, complete densification (~ 100 % relative density) of aluminum was observed. SEM images of spark plasma sintered Al-MG bulk composites discs were presented in Fig. 3.20 (a-f). The figure shows uniform distribution of Fe-based metallic glass in aluminum metal matrix. With the same SPS processing parameters (600 °C, 40 MPa, 10 min) the relative densities of Al-MG composites (as shown in Fig. 3.23) are lower than that for aluminum and decreasing relatively, as the reinforcement content is increasing. The decrease in densification is mainly due to the presence of MG particles which has higher melting point (~1200 °C) and requires higher temperatures and pressures for densification.

The SEM images show a formation of an interfacial reaction between the MG particles and the Al matrix. A circular whitish layer which shows the possibility of reaction between MG and Al is clearly visible in the microstructure in the Al-MG

composites with a different weight percentage of MG as well. The presence of interface between Al and MG results in better bonding between the reinforcement and the matrix which leads to an increase in load-bearing capacity.

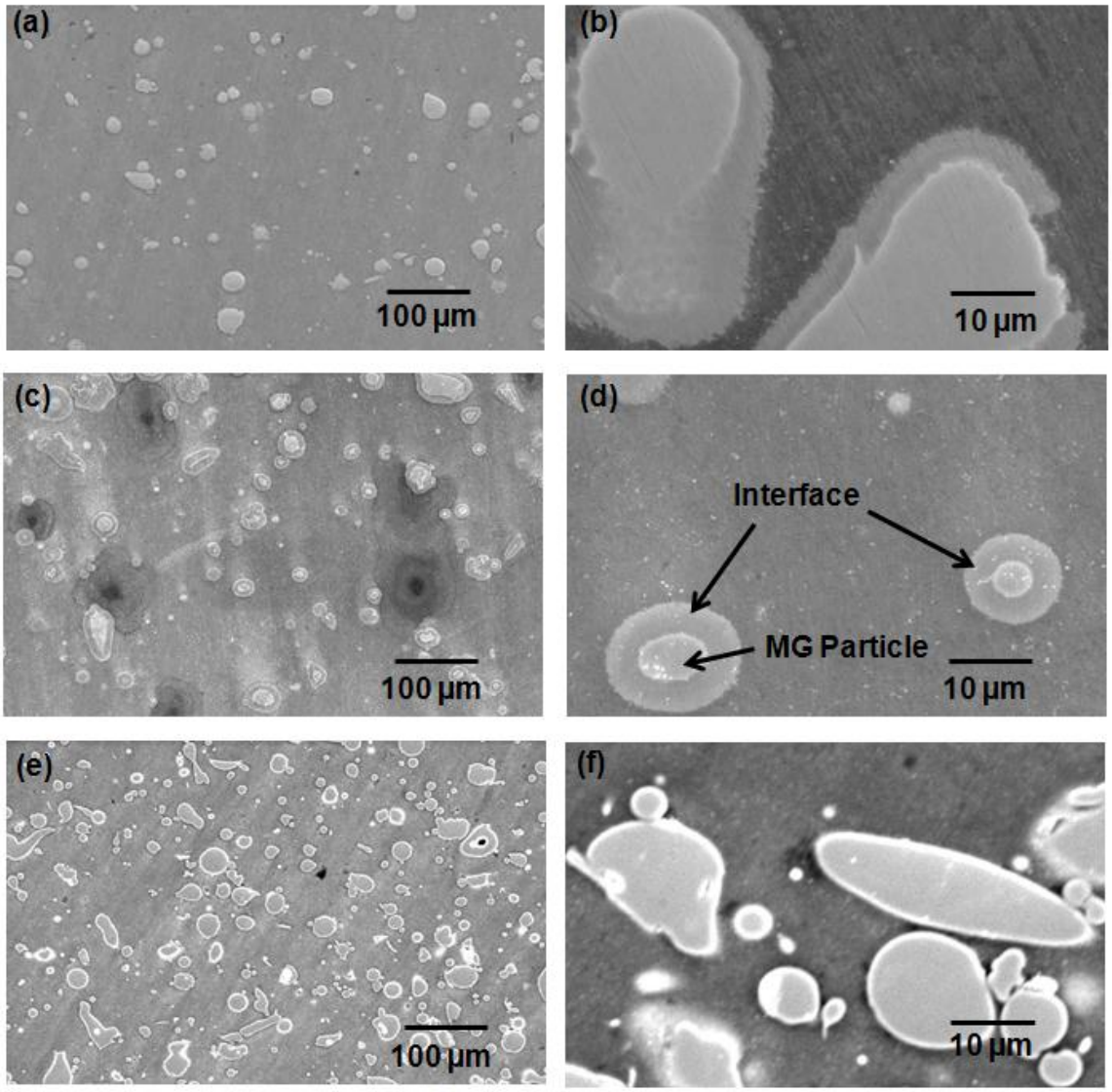

Fig. 3.20 SEM images of spark plasma sintered Al-MG composites with reinforcement of (a-b) 5 wt.% , (c-d) 10 wt.%, and (e-f) 20 wt.% MG

In order to have better understanding regarding the interface present between Aluminum and MG particles, EDS analysis were performed. Fig. 3.21 shows line scan and Fig. 3.22 shows area scan of the interface.

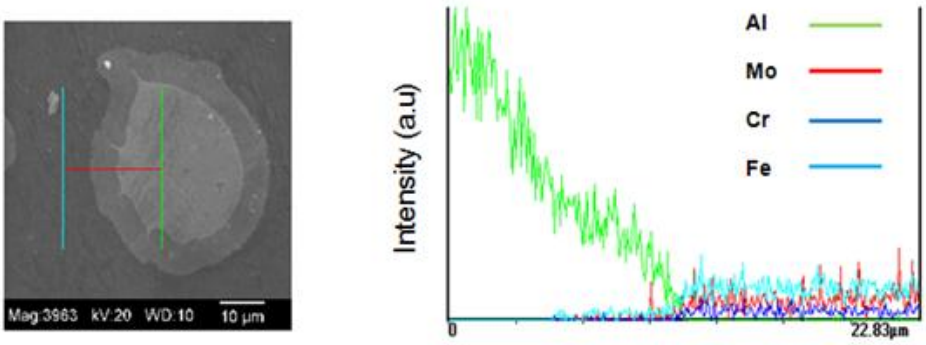

Fig. 3.21 Line scans analysis of interface between aluminum and MG particles

Line scan clearly shows the presence of both Aluminum as well as constituents of MG alloy. In addition, line scan clearly shows decrease in Al content as it reaches MG particle. Similar distribution is present in area scan also, which gives a clear image of the constituents of the interface.

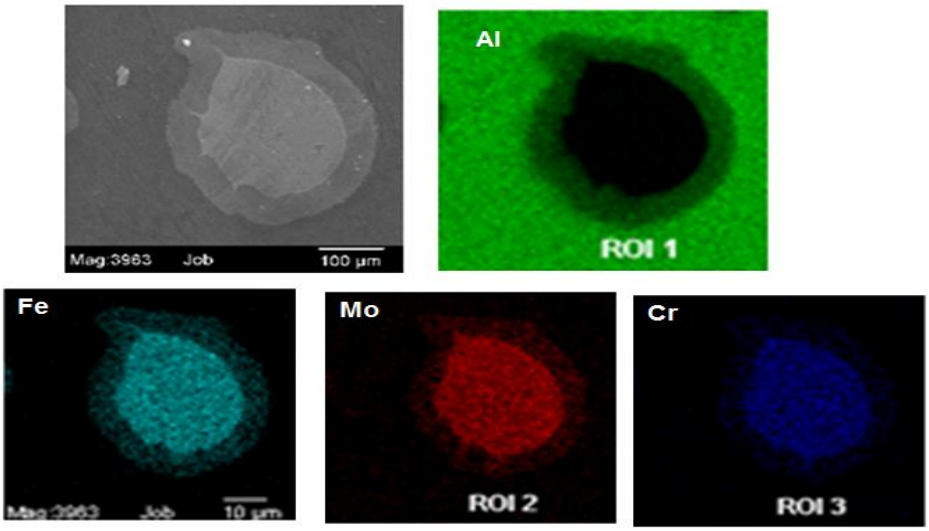

Fig. 3.22 Area scans analysis of interface between aluminum and MG particles

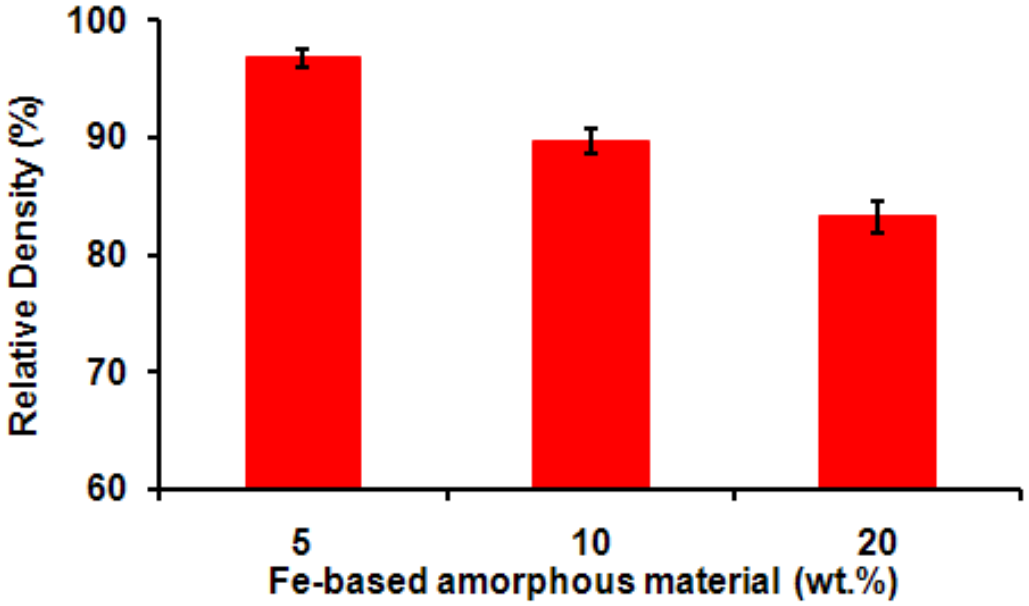

Fig. 3.23 Relative densities of spark plasma sintered Al-MG composites with reinforcement of 5, 10, and 20 wt.% MG

X-ray diffraction (XRD) patterns from the spark plasma sintered Al-MG composites are presented in Fig. 3.24. XRD patterns showed primary aluminum peaks. The broad halo peak which is characteristic of metallic glasses was not observed in Al-5 wt.% MG and Al-10 wt.% MG. However, it is seen in Al-20 wt.% MG. It is observed due to the high content of Fe-based metallic glass powder in the aluminum matrix. For the sample sintered at Al-20 wt.% MG composites, a peak corresponding to $Al_{91}Fe_4Cr_5$ phase is observed. This phase is formed due to interfacial reaction between the MG and the Al. It has an icosahedral quasi crystalline phase, which is not studied much.

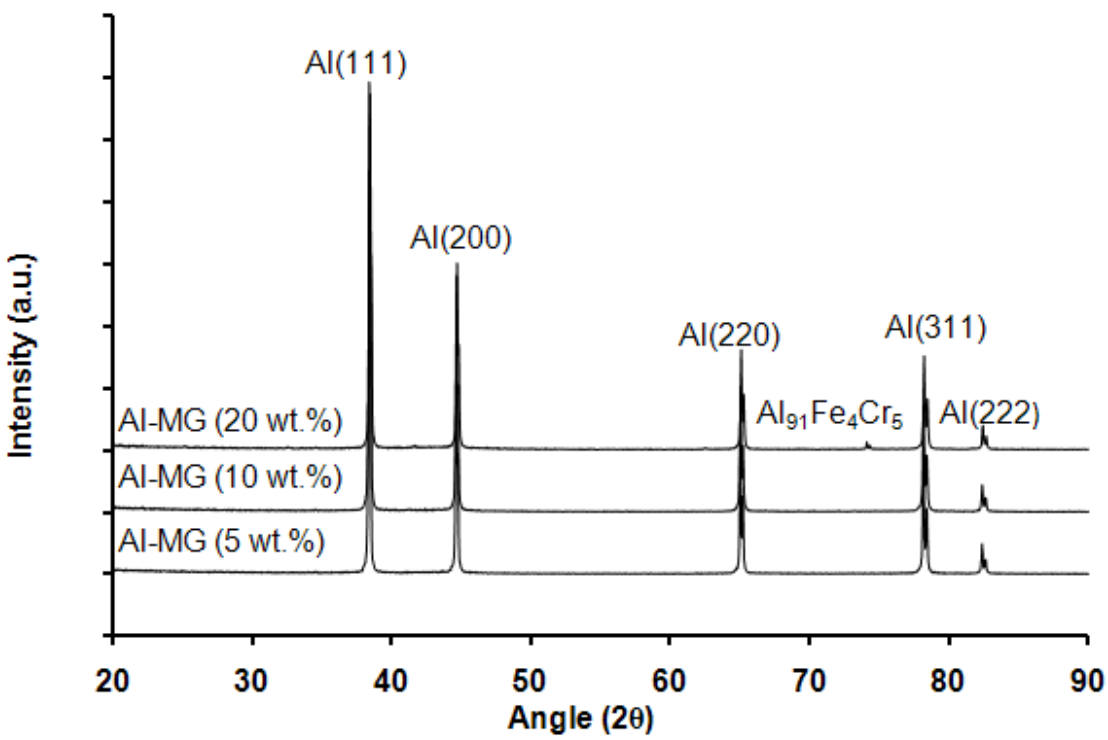

Fig. 3.24 X-ray diffraction patterns from spark plasma sintered Al-MG composites with reinforcement of 5, 10, and 20 wt.% MG

3.3.2 Microhardness

The average microhardness of Al-MG composites with 5, 10, and 20 wt.% MG were found to be 37 (±3), 41 (±4), and 44 (±3) HV, respectively (as shown in Fig. 3.25). With similar SPS processing parameters, the average microhardness of aluminum was found to be 36 (±4) HV. The microhardness of Al-MG composites shows an increment in hardness of composites with the increment of the content of reinforcement particles. Even though a well distributed MG reinforcement as well as better bonding is shown in the aluminum matrix, a phenomenal increase in the microstructure is not observed. However, there can

be a possibility of increase in the load bearing capacity of these composites during the compression test.

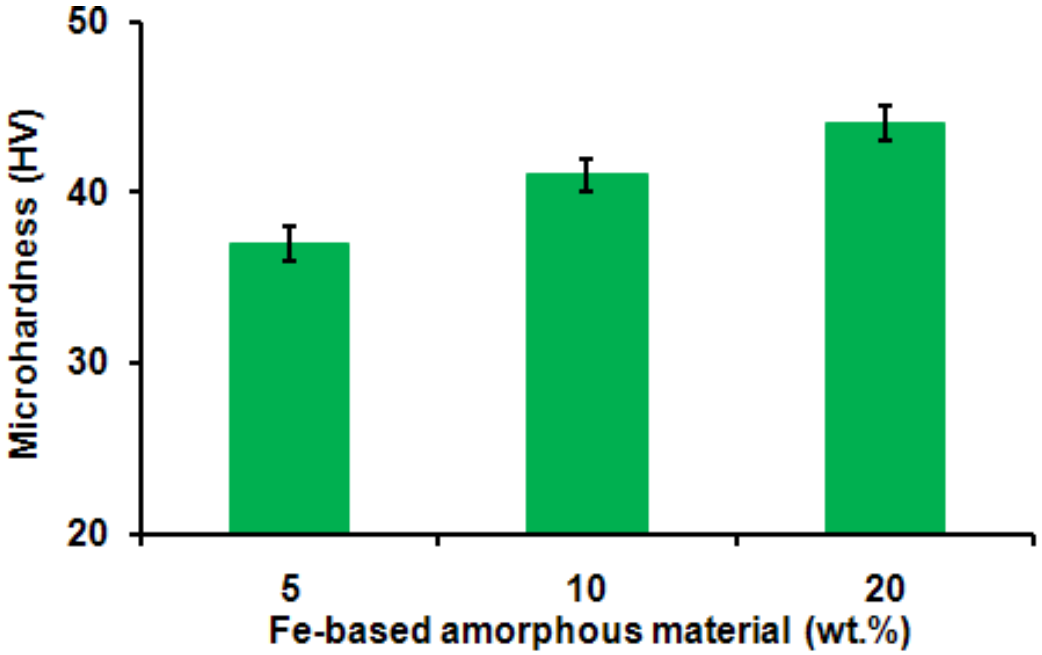

Fig. 3.25 Vickers's microhardness of spark plasma sintered Al-MG composites with reinforcement of 5, 10, and 20 wt.% MG

3.3.3 Wear Characteristics

Fig. 3.26 represents the weight loss as a function of sliding time for aluminum and Al-MG composites during ball-on-disc wear testing conducted with a normal force of 4N. The Al-sample exhibited higher wear weight loss, while the Al-MG composites show a lower wear weight loss. As shown in the weight loss data, weight loss decreased by 1.7 times by reinforcing aluminum with 5 wt.% MG. Similarly, when compared to Aluminum, 2 times and 3 times decrease in weight loss for 10 and 20 wt.% reinforced MG was observed. Increase in wear resistance is mainly due to increase in hardness of the composites.

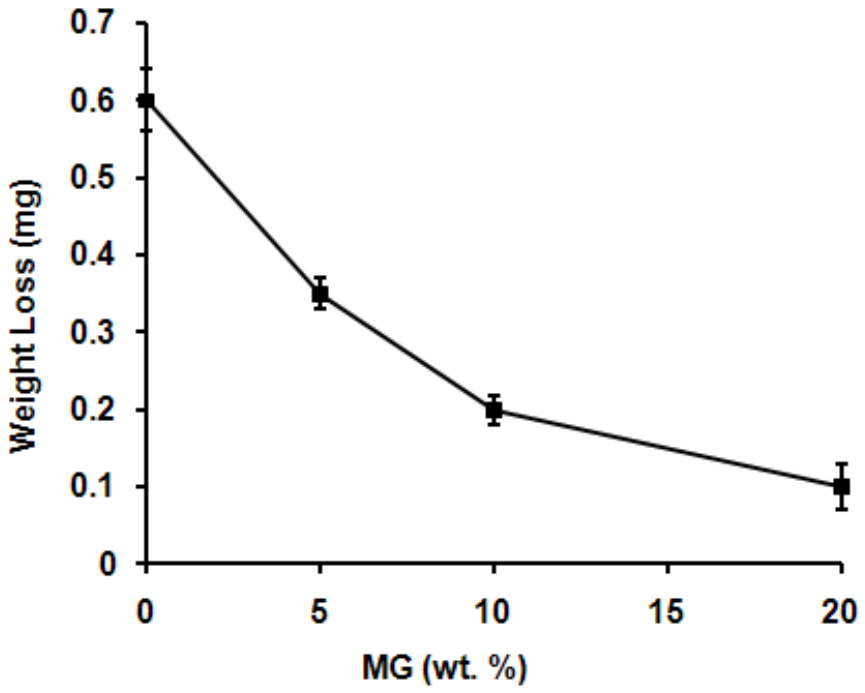

Fig. 3.26 Weight loss as a function of sliding time during ball-on-disc wear testing conducted with normal force of 4 N for aluminum and Al-MG Composites

The variation of coefficient of friction for aluminum and Al-MG composites with reinforcement content of 5, 10, and 20 wt.% is presented in Fig. 3.27. For the aluminum sample, the variation of coefficient of friction was somewhat unpredictable with high values (~ 0.7) in the initial stage (0-3 min) and relatively lower values (~0.5-0.6) in later stages (3-10 min) of the sliding wear test. For the Al-MG composites sample, the coefficient of friction for 5 and 10 wt.% MG reinforcement aluminum composites lie between 0.6 to 0.9 and 0.55 to 0.65, respectively. Some fluctuation can be seen in the Al-MG composites, especially in the case of Al-5 wt.% MG composite. However, the

coefficient of friction for Al- 20 wt.% MG composite is around 0.5, which is relatively less.

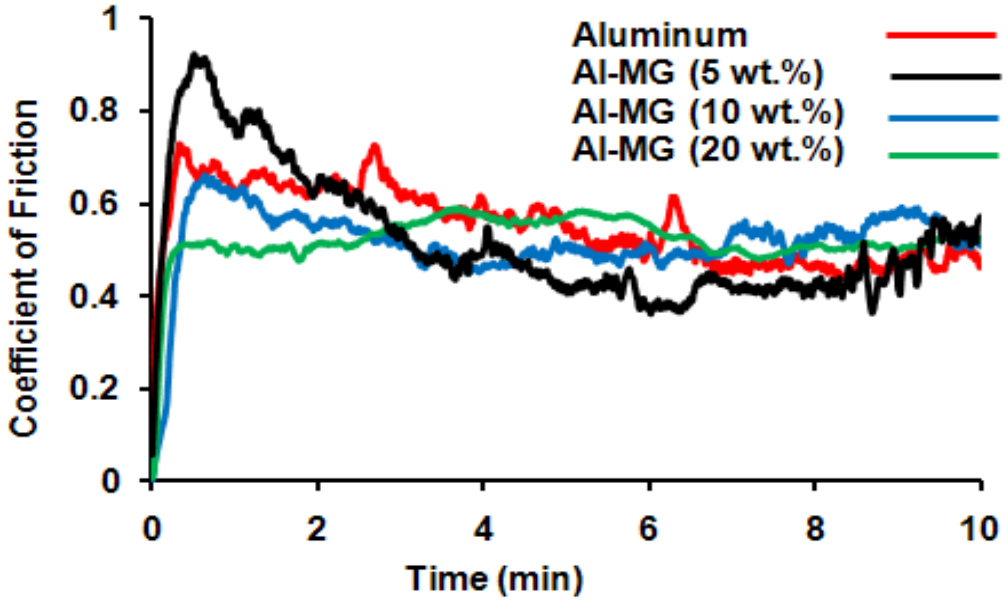

Fig. 3.27 The coefficient of friction with sliding time (10 min) during ball-on-disc wear testing conducted with a normal force of 4 N for aluminum and Al-MG composites

Fig. 3.28 shows profiles of the wear track for Al-MG composites. The wear profile data matches well with the wear loss data. Although the width of the wear track for Al-5 wt.% MG and Al-10 wt.% MG is almost same, there is significant difference between the heights of the wear track which accounts for more wear loss in Al-5 wt.% MG. However, Al- 20 wt.% MG composites shows relatively less width and height of the wear track.

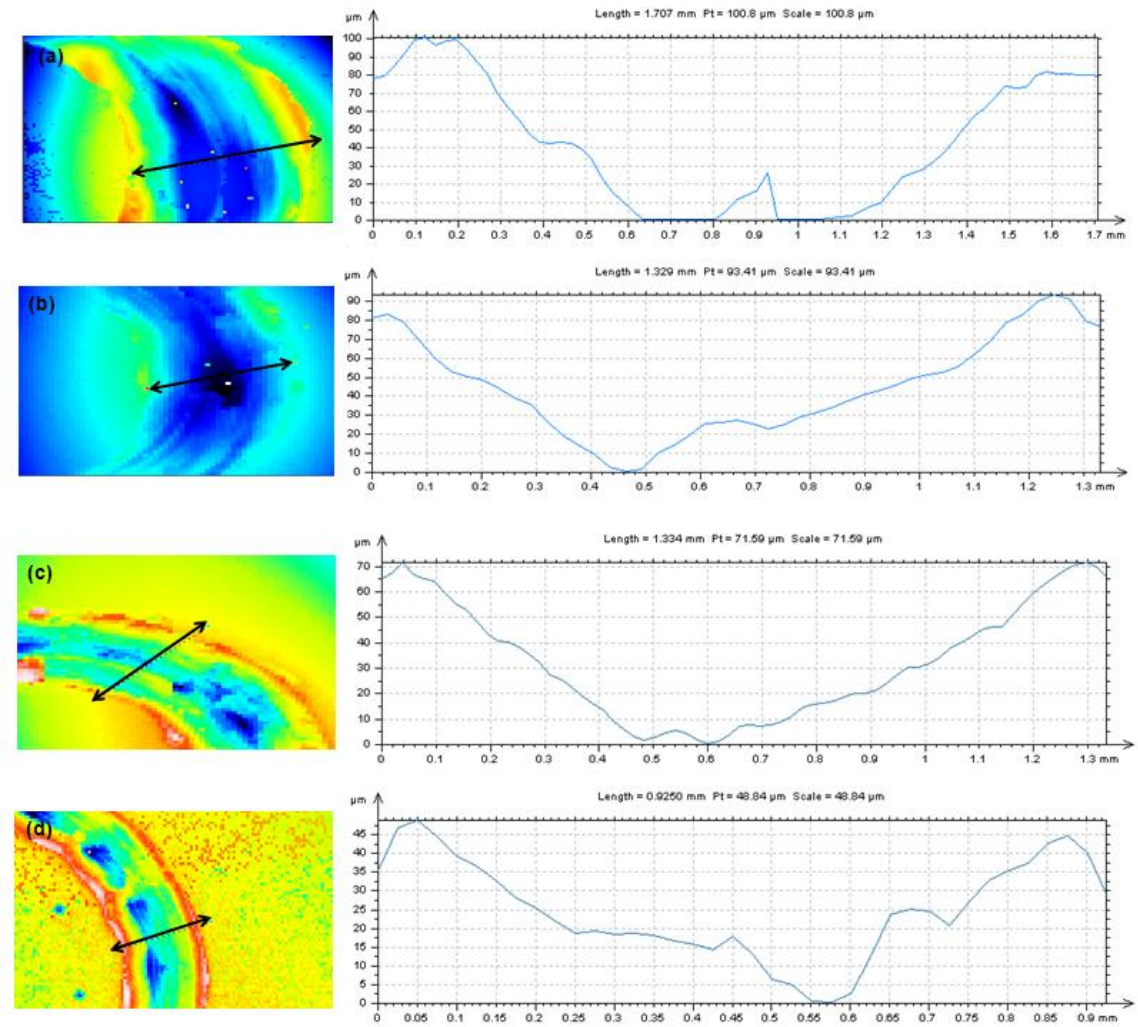

Fig. 3.28 Surface profiles of wear tracks of Al-MG composites (a) pure aluminum (b) 5wt%, (c) 10 wt.%, and (d) 20 wt.% MG

To further investigate the wear mechanism of MG reinforced Al-composites, SEM images of the wear track were analyzed. The presence of microcracks in all the wear track images indicates the strengthening of the matrix during wear. Fig 3.29 (a-f) shows wearing of the MG particle held firmly in the Al matrix. This again shows the strong interface bonding between MG particles and the aluminum matrix.

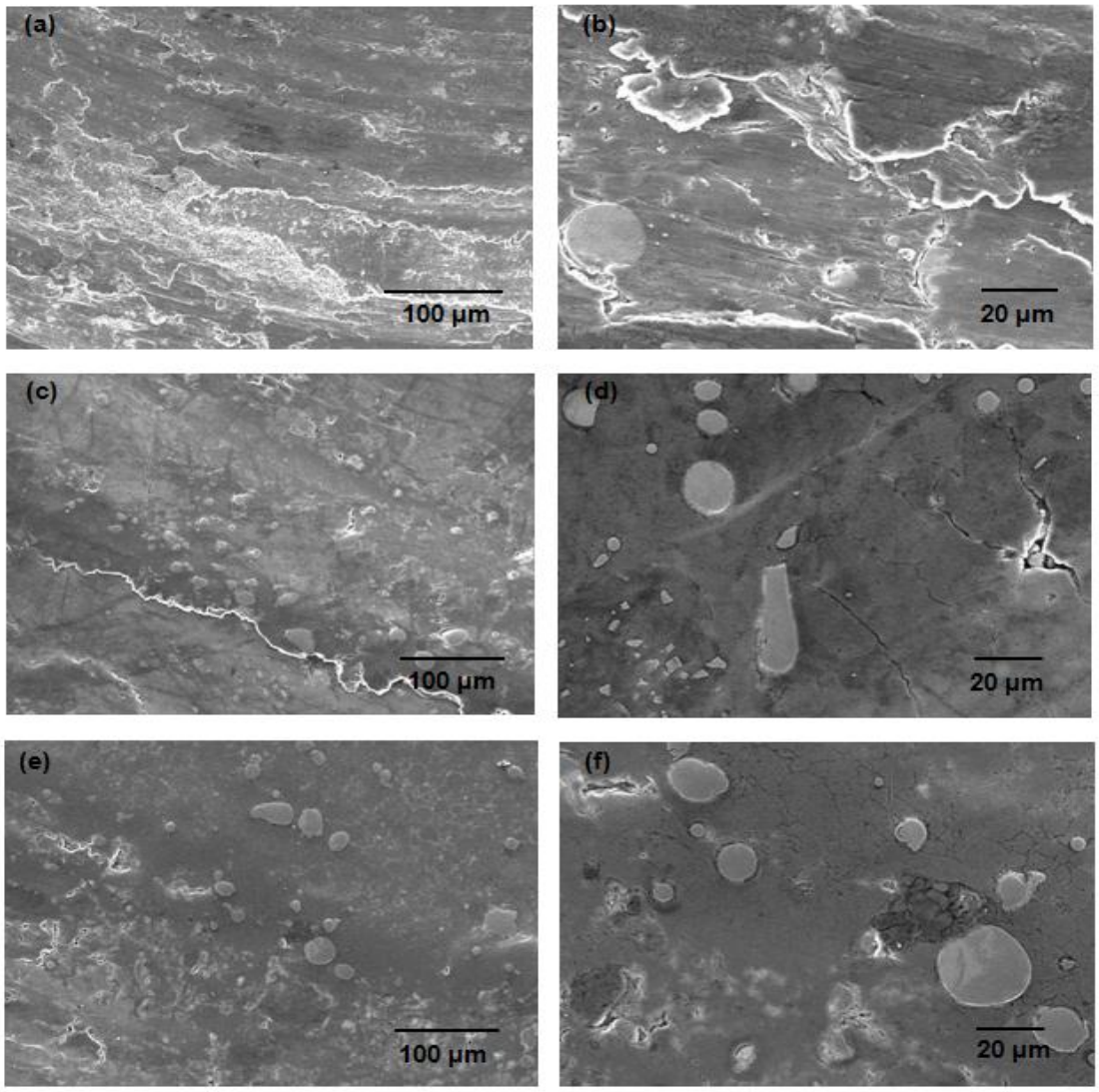

Fig. 3.29 SEM images of wear track of spark plasma sintered Al-MG composites with reinforcement of (a-b) 5 wt.% , (c-d) 10 wt.%, and (e-f) 20 wt.% MG

CHAPTER 4

CONCLUSIONS

- Spark plasma sintering of aluminum powder at sintering temperature results in highly dense (~ 100%) bulk sample.
- Aluminum matrix composites were successfully fabricated using SPS. Nearly, full densifications of the aluminum matrix composites were observed.
- Ball milling of Al-CNT mixture with polyacrylic acid (PAA) followed by spark plasma sintering (SPS) at 600 ºC for 10 minutes resulted in fairly uniform distribution of CNTs in the aluminum matrix composites.
- No interfacial reaction with the formation of Al_4C_3 was observed during SPS of Al-CNT composites.
- In Al-CNT composites, significant improvement in micro-hardness, nano-hardness, and compressive yield strength was observed.
- The Al-CNT composites further exhibited improved wear resistance and lower friction coefficient due to strengthening and self-lubricating effects of CNTs.
- BMG of 5 wt.%, 10 wt.%, and 20 wt.% were reinforced in the aluminum matrix using spark plasma sintering.
- Due to presence of high melting point Fe-based metallic glass powder particles and difference in size particles, influenced the densification characteristics of the

composite powders. Reinforcing MG resulted in increase in micro-hardness and wear resistance.

- 5 wt.%, 10 wt.%, and 20 wt.% of SiC were reinforced in the aluminum matrix using spark plasma sintering. Reinforcing SiC resulted in increase in micro-hardness and wear resistance.

CHAPTER 5

FUTURE WORKS

- To understand the interfacial properties between aluminum and MWCNT composites using transmission electron microscopy (TEM) and Raman spectroscopy analysis.
- To perform detailed corrosion analysis of aluminum matrix composites.
- To make net shapes of Al-matrix composites using spark plasma sintering.
- To investigate the thermal conductivity of Al-matrix composites.

REFERENCES

1. J. E. Hatch, *Aluminum Association, American Society for metals*, **2005**, 1.
2. K. K. Chawla, N. Chawla, *John Wiley & Sons, Inc.* **2000**, 16, 137.
3. K. Anthony, *J. Mater. Sci*. **2006**, 41, 905.
4. M. Surappa, *Sadhana* **2003**, 28, 319.
5. N. Chawla, Y. L. Shen, *Adv Eng Mater* **2001**, 6, 3.
6. Y. T. Zhu, W. R. Blumenthal, T. C. Loew, *J. Mater. Sci.* **1997**, 32, 2037.
7. J. M. Papazian, P. N. Adler, *Metall. Mater. Trans. A* **1990**, 21, 401.
8. F. A. Girot, J.M. Quenisset**,** R. Naslain, *Compos. Sci. Technol*. **1987**, 30, 155.
9. W. Zhang, M. Gu, J. Chen, Z. Wu, F. Zhang, H. E. Deve, Mater. Sci. Eng., A **2003**, 341, 9.
10. http://www.b2b-powder-metallurgy.com/gear-parts-1.htm, May 15th **2011**.
11. V. Viswanathan, T. Laha, K. Balani, A. Agarwal, S. Seal, *Mater. Sci. Eng., R* **2006**, 54, 121.
12. H. J. Choi, G. B. Kwon, G. Y. Lee, D. H. Bae, *Scr. Mater.* **2008**, 59, 360.
13. J. Z. Liao, M. J. Tan, I. Sridhar, *Mater. Des.* **2010**, 31, 96.
14. H. Kwon, M. Estili, K. Takagi, T. Miyazaki, A. Kawasaki, *Carbon* **2009**, 47, 570.
15. A.K. Ghosh, S. Suresh, A. Mortensen, A. Needleman, *Fundamentals of Metal Matrix Composites* **1993**, 121.

16. N. H. Kim, C. G. Kong, B. M. Kim, *Int. J. Mech. Sci.* **2001**, 43, 1507.

17. A. Zulfia, H. V. Atkinson, H. Jones, S. King, *J. Mater. Sci.* **1999**, 34, 4305.

18. H. V. Atkinson, A. Zulfia, A. L. Filho, H. Jones, S. King, *Mater. Des.* **1997**, 18, 243.

19. Z. M. Xu, N. L. Loh, W. Zhou, *J. Mater. Process. Technol.* 1997, 67, 131.

20. D. Roy, S. Ghosh, A. Basumallick, B. Basu, *Mater. Sci. Eng., A* **2006**, 415, 202.

21. W. L. Zhang, M. Y. Gu, D. Z. Wang, Z. K. Yao, *Mater. Lett.* **2004**, 58, 3414.

22. M. Bagheripoor, H. Bisadi, *Appl. Therm. Eng.* **2011**, 31, 1556.

23. W. D. Fei, W. Z. Li, C. K. Yao, *J. Mater. Sci.* **2002**, 37, 211.

24. S. C. Xu, L. D. Wang, P. T. Zhao, W. L. Li, Z. W. Xue, W. D. Fei, *Mater. Sci. Eng., A* **2011**, 528, 3243.

25. K. Sukumaran, K. K. Ravikumar, S. G. K. Pillai, T. P. D. Rajan, M. Ravi, R. M. Pillai, B. C. Pai, *Mater. Sci. Eng., A* **2008**, 490, 235.

26. I. A. Ibrahim, F. A. Mohamed, E. J. Lavernia, *J. Mater. Sci.* **1991**, 26, 1137.

27. C. G. Kang, K. S. Yun, *J. Mater. Process. Technol.* **1996**, 62, 116.

28. Q. Li, C. A. Rottmair, R. F. Singer, *Compos. Sci. Technol.* **2010**, 70, 2242.

29. T. R. Vijayaram, S. Sulaiman, A. M. S. Hamouda, M. H. M. Ahmad, *J. Mater. Process. Technol.* **2006**, 178, 34.

30. M. S. Yong, A. J. Clegg, *J. Mater. Process. Technol.* **2005**, 168, 262.

31. P. Poddar, V. C. Srivastava, P. K. De, K. L. Sahoo, *Mater. Sci. Eng., A* **2007**, 460, 357.

32. J. Hashim, L. Looney, M. S. J. Hashmi, *J. Mater. Process. Technol.* **1999**, 92, 1.

33. T. P. D. Rajan, R. M. Pillai, B. C. Pai, K. G. Satyanarayana, P. K. Rohatgi, *Compos. Sci. Technol.* **2007**, 67, 3369.

34. E. Neubauer, M. Kitzmantel, M. Hulman, P. Angerer, *Compos. Sci. Technol.* **2010**, 70, 2228.

35. Y. Feng, H. L. Yuan, M. Zhang, *Mater. Char.* **2005**, 55, 211.

36. Y. Tang, H. Cong, R. Zhong, H. M. Cheng, *Carbon* **2004**, 42, 3260.

37. W. X. Chen, J. P. Tu, L. Y. Wang, H. Y. Gan, Z. D. Xu, X. B. Zhang, *Carbon* **2003**, 41, 215.

38. X. L. Shi, H. Yang, G. Q. Shao, X. L. Duan, L. Yan, Z. Xiong, P. Sun, *Mater. Sci. Eng., A* **2006**, 457, 18.

39. T. P. D. Rajan, R. M. Pillai, B. C. Pai, K. G. Satyanarayana, P. K. Rohatgi, *Compos. Sci. Technol.* **2007**, 67, 3369.

40. M. Tokita, *In Proceedings of the International Symposium on Microwave, Plasma and Thermochemcial Processing of Advanced Materials*, ed S. Miyake and M. Samandi. JWRI, Osaka Universities Japan, **1997**, 69.

41. G R. Orru, R. Licheri, A. M. Locci, A. Cincotti, G. Cao, *Mater. Sci. Eng., R* **2009**, 63, 127.

42. Z. A. Muneer, U. Anselmi-Tamburini, M. Ohyanagi, *J. Mater. Sci*. **2006**, 41, 763.

43. A. Robert, *Ceramic Industry magazine* **2008.**

44. J. E. Garay, *Annu. Rev. Mater. Res.* **2010**, 40, 445.

45. E. A. Olevsky, S. Kandukuri, L. Froyen, *J. Appl. Phys.* **2007**, 102, 114913.

46. G. Xie, O. Ohashi, K. Chiba, N. Yamaguchi, M. Song, K. Furuya, T. Noda, *Mater. Sci. Eng., A* **2003**, 359, 384.

47. U. Anselmi-Tamburini, J. E. Garay, Z. A. Munir, *Mater. Sci. Eng., A* **2005**, 407, 24.

48. S. Iijima, *Nature* **1991**, 354, 56.

49. J. Y. Huang, S. Chen, Z. Q. Wang, K. Kempa, Y. M. Wang, S. H. Jo, G. Chen, M. S. Dresselhaus, Z. F. Ren, *Nature* **2006**, 439, 281.

50. E. W. Wong, *Science* **1997**, 277, 1971.

51. C. N. R. Rao, *Chem. Phys.* **2001**, 2, 78.

52. S. Subramoney, *Adv. Mater.* **1998**, 10, 1157.

53. I. Y. Kim, J. H. Lee, J. S. Lee, S. H. Baik, Y. J. Kim, Y. Z. Lee, *Wear* **2009**, 267, 593.

54. M. S. P. Shaffer, A. H. Windle, *Adv. Mater.* **1999**, 11, 937.

55. X. Y. Gong, J. Liu, S. Baskaran, R. D. Voise, J. S. Young, *Chem. Mater.* **2000**, 12, 1049.

56. E. Carreno-Morelli, *Carbon Nanotube-Metal Matrix Composites*, The Dekker Encyclopedia of Nanoscience and Nanotechnology, Taylor and Francis, New York, **2006**.

57. T. Nogochi, A. Magario, S. Fukazawa, S. Shimizu, J. Beppu, M. Seki, *Mater. Trans., JIM* **2004**, 45, 602.

58. C. F. Deng, D. Z. Wang, X. X. Zhang, A. B. Li, *Mater. Sci. Eng., A* **2007**, 444, 138.

59. A. M. K. Esawi, K. Morsi, A. Sayed, A. Abdel Gawad, P. Borah, *Mater. Sci. Eng., A* **2009**, 508, 167.

60. Q. Li, C. A. Rottmair, R. F. Singer, *Compos. Sci. Technol.* **2010**, 70, 2242.

61. B. Abbasipour, B. Niroumand, S. M. Monir Vaghefi, *Trans. Nonferrous Met. Soc. China* **2010**, 20, 1561.

62. S. R. Bakshi, V. Singh, S. Seal, A. Agarwal, *Surf. Coat. Technol.* **2009**, 203 1544.

63. S. R. Bakshi, A. K. Keshri, V. Singh, S. Seal, A. Agarwal, *J. Alloys Compd.* **2009**, 481, 207.

64. X. Wang, X. Cai, *Adv. Mater. Res.* **2010**, 150, 1163.

65. G. George, K.T. Kashyap, R. Rahul, Y. Yamdagni, *Scripta Mater.* **2005**, 53, 1159.

66. I. Kim, J. Hee, G. Lee, S. Baik, Y. Kim, Y. Lee, *Wear* **2009**, 269, 593.

67. H. J. Choi, G. B. Kwon, G.Y. Lee, D. H. Bae, *Scripta Mater*. **2008**, 59, 360.

68. J. Jiang, H. Wang, H. Yang, J. Xu, *Trans. Nonferrous Met. Soc. China*, **2007**, 17, 113.

69. R. Perez-Bustamante, I. Estrada-Guel, W. Antunez-Flores, M. Miki-Yoshida, P. J. Ferreira, R. Martinez-Sanchez, *J. Alloys Compd.* **2008**, 450, 323.

70. R. Perez-Bustamante, I. Estrada-Guel, P. Amezaga-Madrid, M. Miki-Yoshida, *J. Alloys Compd.* **2010**, 495, 399.

71. A. M. K. Esawi, K. Morsi, A. Sayed, M. Taher, S. Lanka, *Compos. Sci. Technol.* **2010**, 70, 2237.

72. K. Morsi, A. M. K. Esawi, P. Borah, S. Lanka, A. Sayed, *J. Compos. Mater.* **2010**, 44, 1991.

73. L. Jin-Zhi, T. Ming-Jen, S. Idapalapati, *Mater. Des.* **2010**, 31, 96.

74. K. Morsi, A. M. K. Esawi, S. Lanka, A. Sayed, M. Taher, *Composites Part A* **2010**, 41, 322.

75. H. Prielipp, M. Knechtel, N. Claussen, S. K. Streiffer, H. Mullejans, M. Ruhle, J. Rodel, *Mater. Sci. Eng., A* **1995**, 197, 19.

76. M. K. Surappa, P. K. Rohatgi, *J. Mater. Sci.* **1981**, 16, 983.

77. R. M. Mohanty, K. Balasubramanian, S. K. Seshadri, *Mater. Sci. Eng., A* **2008**, 498, 42.

78. S. Hashimoto, A. Yamaguchi, M. Koshino, *Mater. Sci. Eng., A* **1999**, 265, 71.

79. M. A. Taha, *Mater. Des*. **2001**, 22, 431.

80. N. H. Tran, A. S. Milev, M. A. Wilson, J. R. Bartlett, G. S. K. Kannangara, *Surf. Interface Anal.* **2008**, 40, 1294.

81. L. Ci, Z. Ryu, N.Y. Jin-Phillipp, M. Ruhle, *Acta Mater*. **2006**, 54, 5367.

82. G. M. Pharr, *Mater. Sci. Eng., A* **1998**, 253,151.

83. W. C. Oliver, G. M. Pharr, *J. Mater. Res*. **1992**, 7, 1564.

APPPENDICES

PUBLICATION

Vineet Yadav, Sandip P. Harimkar, Microstructure and Properties of Spark Plasma Sintered Carbon Nanotube Reinforced Aluminum Matrix Composites, *Advanced Engineering Materials*, accepted for publication **2011**.

PRESENTATION

Fabrication and characterization of MWCNT reinforced aluminum composite using Spark Plasma Sintering (Presented at TMS-2011 International Conference at San-Diego, CA, USA).

VITA

Vineet Yadav

Candidate for the Degree of

Master of Science

Thesis: SPARK PLASMA SINTERING OF ALUMINUM MATRIX COMPOSITES

Major Field: Mechanical and Aerospace Engineering

Biographical:

Personal Data: Born in Guna, MP on July 01, 1985; Son of Mr. Chandra Shekhar Yadav and Mrs. Usha Yadav

Education:

Completed the requirements for the Master of Science in Mechanical and Aerospace Engineering at Oklahoma State University, Stillwater, Oklahoma, in July, 2011.

Completed the requirements for the Bachelor of Engineering in Mechanical Engineering at Rajiv Gandhi Technical University, Bhopal, India in 2007.

Experience:

Has one year of experience as process engineer and worked on seamless steel tubes. More than 2 years of experience in processing of nanocrystalline materials using Spark plasma sintering. Author one international journal paper and has expertise in characterizations of aluminum matrix composites.

Professional Memberships:

The Minerals, Metals & Materials Society (TMS), Association for Iron and Steel Technology (AIST), The American Ceramic Society (ACerS), ASM International (The Materials Information Society).

Name: Vineet Yadav Date of Degree: July, 2011

Institution: Oklahoma State University Location: Stillwater, Oklahoma

Title of Study: SPARK PLASMA SINTERING OF ALUMINUM MATRIX COMPOSITES

Pages in Study: 90 Candidate for the Degree of Master of Science

Major Field: Mechanical and Aerospace Engineering

Aluminum matrix composites make a distinct category of advanced engineering materials having superior properties over conventional aluminum alloys. Aluminum matrix composites exhibit high hardness, yield strength, and excellent wear and corrosion resistance. Due to these attractive properties, aluminum matrix composites materials have many structural applications in the automotive and the aerospace industries. In this thesis, efforts are made to process high strength aluminum matrix composites which can be useful in the applications of light weight and strong materials.

Spark Plasma Sintering (SPS) is a relatively novel process where powder mixture is consolidated under the simultaneous influence of uniaxial pressure and pulsed direct current. In this work, SPS was used to process aluminum matrix composites having three different reinforcements: multi-wall carbon nanotubes (MWCNTs), silicon carbide (SiC), and iron-based metallic glass (MG). In Al-CNT composites, significant improvement in micro-hardness, nano-hardness, and compressive yield strength was observed. The Al-CNT composites further exhibited improved wear resistance and lower friction coefficient due to strengthening and self-lubricating effects of CNTs. In Al-SiC and Al-MG composites, microstructure, densification, and tribological behaviors were also studied. Reinforcing MG and SiC also resulted in increase in micro-hardness and wear resistance.

ADVISER'S APPROVAL: Dr. Sandip P. Harimkar